Nitride or Oxynitride? Elucidating the Composition-Activity Relationships in Molybdenum Nitride Electrocatalysts for the Oxygen Reduction Reaction

Melissa E. Kreider*[1,2], Michaela Burke Stevens*[1,2], Yunhzi Liu[3], Anjli M. Patel[1,2], Michael J. Statt[1,2], Brenna M. Gibbons[2,3], Alessandro Gallo[2,4], Micha Ben-Naim[1,2], Apurva Mehta[4,5], Ryan C. Davis[4,5], Anton V. Ievlev[6], Jens K. Nørskov[7], Robert Sinclair[3], Laurie A. King[8], Thomas F. Jaramillo[1,2]

1) Department of Chemical Engineering, Stanford University 443 Via Ortega, Stanford, CA 94305, USA

2) SUNCAT Center for Interface Science and Catalysis, SLAC National Accelerator Laboratory, Menlo Park, CA 94025, USA

3) Material Science and Engineering, Stanford University, 496 Lomita Mall, Stanford, CA 94305, USA

4) SLAC National Accelerator Laboratory, 2575 Sand Hill Road, Menlo Park, CA, USA

5) Stanford Synchrotron Radiation Lightsource, SLAC National Accelerator Laboratory, Menlo Park, CA 94025, USA

6) Center for Nanophase Materials Sciences, Oakridge National Laboratory, Oak Ridge, TN 37831, USA

7) Department of Physics, Technical University of Denmark, 2800 Kongens Lyngby, Denmark

8) Faculty of Science and Engineering, Manchester Metropolitan University, Chester Street, Manchester, M1 5GD, UK

*these authors contributed equally

Corresponding authors: l.king@mmu.ac.uk and jaramillo@stanford.edu

ABSTRACT

Molybdenum nitride (Mo-N) catalysts have shown promising activity and stability for the oxygen reduction reaction (ORR) in acid. However, the effect of oxygen (O) incorporation (from synthesis, catalysis, or exposure to air) on their activity remains elusive. Here we use reactive sputtering to synthesize three compositions of thin film catalysts and use extensive materials characterization to investigate the depth-dependent structure and incorporated O. We show that the as deposited Mo-N films are highly oxidized both at the surface (>30% O) and in the bulk (3-21% O) and that the ORR performance is strongly correlated with the bulk structure and composition. Activity for $4e^-$ ORR is highest for compositions with the highest N:O and N:Mo ratio. Furthermore, H_2O_2 production for the films with moderate O content is comparable to or higher than the most H_2O_2-selective non-precious metal catalysts in acidic electrolyte, on a moles per mass or surface area of catalyst basis. Density functional theory provides insight into the energetics of O incorporation and vacancy formation, and we hypothesize that activity trends with O:N ratios can be traced to the varying crystallite phases and their interactions with ORR

adsorbates. This work demonstrates the prevalence and significance of O in metal nitride electrocatalysts and motivates further investigation into the role of O in other non-precious metal materials.

1.0 Introduction:

To address the growing energy requirements of the global population as well as to mitigate the impacts of anthropogenically-driven climate change, it is necessary to reduce the world's dependence on fossil fuels and minimize CO_2 emissions. The oxygen reduction reaction (ORR, Equation 1 and 2) is an essential component of many of these carbon-neutral solutions:

$$O_2 + 4H^+ + 4e^- \rightarrow 2H_2O \qquad E = 1.229 \text{ V vs RHE} \qquad [1]$$

$$O_2 + 2H^+ + 2e^- \rightarrow H_2O_2 \qquad E = 0.695 \text{ V vs RHE} \qquad [2]$$

Specifically, $4e^-$ ORR (Equation 1) is the cathodic reaction for polymer electrolyte membrane fuel cells (PEMFCs), which can use hydrogen as a carbon-free fuel to produce power. PEMFCs offer a promising route towards the decarbonization of a variety of sectors, including transportation and stationary, portable, and emergency backup power.[1,2] In the transportation sector, PEMFCs offer several benefits over internal combustion engines, including efficiencies up to 60% and the potential for substantially mitigated greenhouse gas emissions.[3,4] Other technologies, such as rechargeable metal-air batteries, also rely on the ORR. These batteries are promising for a variety of applications due to their superior specific capacity and energy density relative to commercial Li-ion batteries.[5–8] For PEMFCs, substantial platinum catalyst loadings are required to overcome the slow ORR kinetics and resulting high overpotentials.[9–12] The widespread development of PEMFCs is therefore limited by the scarcity and high price of these platinum-based catalysts.[13–15]

Beyond energy conversion technologies, $2e^-$ ORR (Equation 2) is also of interest as an electrochemical route to the synthesis of hydrogen peroxide (H_2O_2), an important commodity chemical used for chemical synthesis, bleaching, disinfecting, and industrial waste treatment.[16] Currently H_2O_2 is produced industrially at large scales, but a decentralized electrochemical synthesis would be desirable to avoid costs (economic and environmental) associated with transportation and instability.[17] Developing active and selective non-precious metal ORR catalysts is thus of critical importance for the deployment of several green technologies.[18,19]

Transition metal-nitrogen-carbon (M-N-C) materials are among the most promising platinum group metal-free (PGM-free) ORR catalysts.[15,20,21] Specifically, Fe-N-C and Co-N-C catalysts have shown activities approaching that of Pt and in-depth characterization has been used to provide insight to design more active M-N_xC moieties.[22–26] While Pt-like performance has been achieved in a PEMFC configuration, their lower ORR $4e^-$ selectivity (Equation 1) and concerns regarding catalyst stability have complicated commercial application to date.[27,28] Carbon corrosion has been identified as one of the major degradation mechanisms and carbon oxidation at higher potentials means that the more active catalysts are more susceptible to rapid degradation.[29] As potentially carbon-free alternatives to the M-N-Cs, transition metal nitrides (TMNs) are a promising class of electrocatalysts owing to their earth abundance, conductivity, and corrosion-resistance in acid.[30–

[33] However, their ORR performance to date has not matched that of the M-N-C catalysts. In order to design TMNs with enhanced ORR performance it is necessary to understand the role of composition and structure in $2e^-$ and $4e^-$ activity.

Various phases of molybdenum nitride (Mo-N) single-metal and mixed-metal nanoparticulate catalysts have shown promising ORR activity and stability.[34,35] However, while these and other works have thoroughly described the role that the bulk and average crystal structure and Mo coordination plays in activity, there is very little understanding of the role that O, a common nitride contaminant,[36] plays in activity or selectivity. Furthermore, previous studies on non-Mo metal oxy(carbo)nitride nanoparticles have indicated that the degree of oxidation has important impacts on ORR activity. For TaOCN[37], TiOCN[38], and ZrOCN[39] nanoparticles, it has been shown that the ORR activity could be tuned by changing the degree of oxidation and vacancies were cited as an important mechanism for enhancement. Herein we aim to provide a systematic evaluation of the role of O in Mo-N for the ORR with opportunities to extend to a broad range of other systems.

In addition to catalysis, reactively sputtered molybdenum nitride thin films have been extensively studied for various applications, including as hard coatings, superconductors, and diffusion barriers for electronic devices.[40–44] For these applications, precise control of crystal structure and mechanical and electrical properties is desired, and thus the synthesis mechanism has been well-explored and described.[45,46] A variety of structures, including crystalline rocksalt (face-centered cubic lattice, fcc) γ-Mo_2N, tetragonal β-Mo_2N, and hexagonal (hex) δ-MoN as well as amorphous and mixed phase films, have been obtained by modification of substrate temperature, nitrogen partial pressure, and target power during sputtering.[47–50] Further tuning of lattice parameters, N vacancies, and grain size has also been achieved through variation of O partial pressure and total pressure in the sputter chamber due to the strong relationship between composition and formation energy.[51] However, within a compositional range, similar formation energies and the presence of vacancies allows for the stabilization of several different phases simultaneously within a sample. These frequently observed localized compositional or structural gradients motivate extensive characterization on all Mo-N systems synthesized.[52,53]

In this work, we investigate ORR activity trends for a carbon-free molybdenum (oxy)nitride thin film model system. By systematically tuning the synthesis of molybdenum (oxy)nitride thin film catalysts, we probe the effects of structure, composition, and O incorporation on their ORR activity, selectivity, and stability. While structure and N content are found to affect performance, bulk O content is a better predictor of activity. Electrochemical and materials characterization of the film surface reveal substantial changes to the composition, capacitance, and electrochemically active surface area with air exposure. By combining in-depth experimental characterization and theoretical modeling of structure and composition, we report insight into activity trends and demonstrate important design principles for synthesizing active TMN ORR catalysts.

2.0 Results and Discussion

2.1 Bulk and depth-dependent structure and composition of molybdenum (oxy)nitride thin films tuned via reactive sputtering. Nanoparticle Mo-N materials have been previously studied for

electrocatalytic oxygen reduction.[31,35,54] In the nanoparticle configuration it is particularly challenging to understand the structure and composition of the active surface. Complications arise in deconvoluting the roles of the metal nitride catalyst, the carbon support, and O, which may be incorporated intentionally during synthesis or unintentionally from air or during electrocatalysis. To minimize these factors, we synthesized a series of polycrystalline molybdenum (oxy)nitride films with varying N:Mo:O ratios via reactive sputtering. The significant O content observed in these films is indicative of an oxynitride. This technique allows for carbon-free synthesis and control of thickness, composition, and structure by tuning the substrate bias and the N_2 and O_2 partial pressures in the chamber.

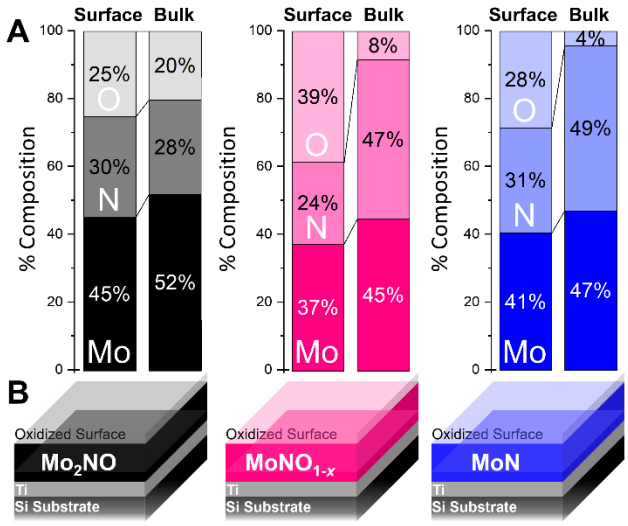

Figure 1. (A) Composition schematic of the as-deposited molybdenum (oxy)nitride films (~ 1 day in air) with (B) corresponding film models. Surface and bulk composition data (% O, N, and Mo) are based on ToF-SIMS depth profiles for one representative sample of Mo_2NO (black), $MoNO_{1-x}$ (pink), and MoN (blue). See Figures S1-2 for details of the composition calculation and ToF-SIMS depth profiles. Samples were in air ≤ 1 week. See Table S1 for more details.

As discussed previously, it is well known that reactively sputtered Mo-N films can form multiple phases concurrently under several reactive sputtering conditions.[45,52] A summary of the reactive sputtering conditions and resulting structures investigated in this work is presented in Table 1. Due to the structural and compositional heterogeneity within the films, the catalysts have been grouped into three different classes based on nominal *bulk* composition: Mo_2NO, $MoNO_{1-x}$, and MoN (Figure 1). The surface and bulk compositions of each film were quantified based on the composition at the top ~ 2 nm and in the middle of the film, respectively, utilizing combined ToF-SIMs depth profile and XPS analysis. Details of the ToF-SIMS calibration via XPS analysis are described in Figure S1.[55] Samples grouped within the same composition range, but with slight variations in synthesis conditions and crystallite structure, have been further denoted with structural labels (e.g. hex for hexagonal, fcc for face centered cubic, and bcc for body centered cubic). These labels are used in the SI. The high O content at the surface is due to oxidation in air, which is discussed further in Section 2.5.

Table 1. Synthesis, composition, and structural metrics for the three compositions of Mo-N thin films (the small structural and synthetic differences within each composition are noted). See Table S1 for details concerning sample air exposure.

		Synthesis Parameters (Reactive Sputtering)			Bulk Composition (XPS/ToF-SIMS)			Structural Expansion (GI-XRD)		Path Lengths (GI-XAS)	
Compositions	Specific Crystallite Structures	N_2 partial pressure (mTorr)	Base Pressure (Torr)	Substrate Bias (V)	N (%)	Mo (%)	O (%)	fcc (111) peak (Å) (Expansion [%])*	hex ($20\bar{2}0$) peak (Å) (Expansion [%])**	Mo-(N) (Å)	Mo-Mo (Å)
MoN	$[MoN]^{hex}_{fcc/bcc}$	6	2.3×10^{-7}	-220	49	47	4	2.38^{+} (-0.9%)	2.50^{+} (0.7%)	2.10	2.89
	$[MoN]^{hex}_{fcc}$	6	5.7×10^{-7}	-110	49	48	3	2.39^{+} (-0.6%)	2.50^{+} (2.3%)	-	-
$MoNO_{1-x}$	$[MoNO_{1-x}]^{hex/fcc}_{bcc}$	6	3.0×10^{-6}	-220	47	45	8	2.39^{+} (-0.6%)	2.51^{+} (1.3%)	2.09	2.87
	$[MoNO_{1-x}]^{hex}_{fcc}$	6	1×10^{-6}	-110	49	43	8	2.39^{+} (-0.6%)	2.52^{+} (1.8%)	-	-
Mo_2NO	$[Mo_2NO]^{fcc}_{bcc}$	1.5	1.2×10^{-6}	0	28	52	20	2.42 (0.7%)	-	2.12	2.86
	$[Mo_2NO]^{fcc}_{fcc}$	1.5	5.7×10^{-7}	0	27	52	21	2.42 (0.6%)	-	-	-

*REF: γ-Mo_2N structure (ICDD 00-025-1366) (111) = 2.404 Å.

**REF: hexagonal δ-MoN (ICDD 00-025-1367) ($20\bar{2}0$) = 2.479 Å.

$^{+}$From peak fit (Figure S3)

The crystal structure of Mo-N strongly influences its material properties and catalytic performance.[35,53] The structures of the MoN, $MoNO_{1-x}$, and Mo_2NO thin films were evaluated using grazing incidence x-ray diffraction (GI-XRD), transmission electron microscopy (TEM), selected area diffraction patterns (SADP) (Figure 2), and grazing incidence X-ray absorption spectroscopy (GI-XAS) (Figures S4-5). By comparing GI-XRD measured at an incidence angle sufficient to probe the bulk of the film (th = 0.5˚, where th is the grazing angle) and SADP of a ~ 30 nm diameter film cross section, we were able to identify the crystal structures within the films. A summary of the structural analysis for each nominal composition is detailed below. Full GI-XRD, TEM, and GI-XAS results for the six film variations are summarized in Figures S3-S11 in the SI.

The nitrogen-poor Mo_2NO films were prepared with a low N_2 partial pressure (1.5 mTorr, 75% Ar, and 25% N_2). Several structures have previously been reported under similar synthesis conditions, including the B1-MoN, γ-Mo_2N, and β-Mo_2N phases.[43,49] In this work, we identify these Mo_2NO films as rocksalt γ-Mo_2N due to the peak profile and lattice constant from GI-XRD, the cubic symmetry observed by TEM (Figure 2A and Figure S7), and the 2:1 Mo:N stoichiometry observed by ToF-SIMS (Figure S2). Specifically, GI-XRD shows diffraction peaks at d-spacings of 2.42, 2.10, 1.48, 1.26, and 1.21 Å corresponding to the (111), (200), (220), (311), and (222) planes of the reference rocksalt γ-Mo_2N structure (Table S2, ICDD 00-025-1366). The a = 4.19 Å lattice parameter calculated from these peaks is consistent with literature values that range between 4.16 – 4.19 Å.[49] The peaks at 1.52 and 1.05 Å are attributed to the Si substrate (Figure S6). The

electron diffraction rings shown in yellow on the SADP overlay with the fcc γ-Mo_2N diffraction peaks (Figure 2A) and fast Fourier transform (FFT) analysis of the high-resolution image shows individual crystallites with fcc symmetry (Figure S7), supporting the structural conclusion from XRD. Scherrer analysis of the XRD peak widths indicates crystallite size of approximately 7 nm (Figure S3). From the ToF-SIMS depth profile (Figure S2), a 2:1 Mo:N ratio with 20% O content is observed in the bulk of the film. To understand the effect of this high O content on Mo oxidation state and ligand environment, Mo K-edge XANES for the bulk of the film (using a grazing incidence angle of 5˚) was compared to Mo metal and oxide standards (Figure S4). The Mo_2NO edge falls between that of the Mo and MoO_3 standards, indicating an intermediate oxidation state. Furthermore, the pre-edge feature, typically observed in an MoO_3 spectrum, is not prominent in the Mo_2NO suggesting that the local coordination is distinct from a typical MoO_3. Fitting of the Mo K-edge EXAFS (Figure S5) shows that the first coordination shell (the shell of elements bonded to the Mo center being probed) is consistent with a Mo-(N/O) bond length of 2.12 Å, which corresponds well with the reference Mo-N bond length of 2.09 Å in the cubic Mo_2N. While it is not possible to distinguish between N and O elements using EXAFS,[56] the standard MoO_3 structures have Mo-O bond lengths between 1.67 – 1.9 Å. The first coordination shell bond length indicates that the O in the system, while substantial, is likely not in a distinct MoO_3 phase, but is rather coordinated similarly to the N (Figure S7). This coordination, together with the lack of molybdenum oxide diffraction peaks in the diffractogram, suggests that the O fills N-vacancies in the γ-Mo_2N rather than forming a phase segregated crystalline or amorphous oxide.[57,58] Duplicates of this composition had slight variations on the Mo_2NO structure due to uncontrollable changes to the O:N partial pressure in the chamber (with the same nominal 25% N_2 partial pressure). Under a higher O_2 partial pressure arising from higher chamber base pressure, a body-centered cubic (bcc) Mo phase forms near the substrate interface, resulting in a new diffraction peak in the bulk at 2.26 Å that corresponds to the (110) plane of bcc Mo (ICDD 00-042-1120) (Figure S3).

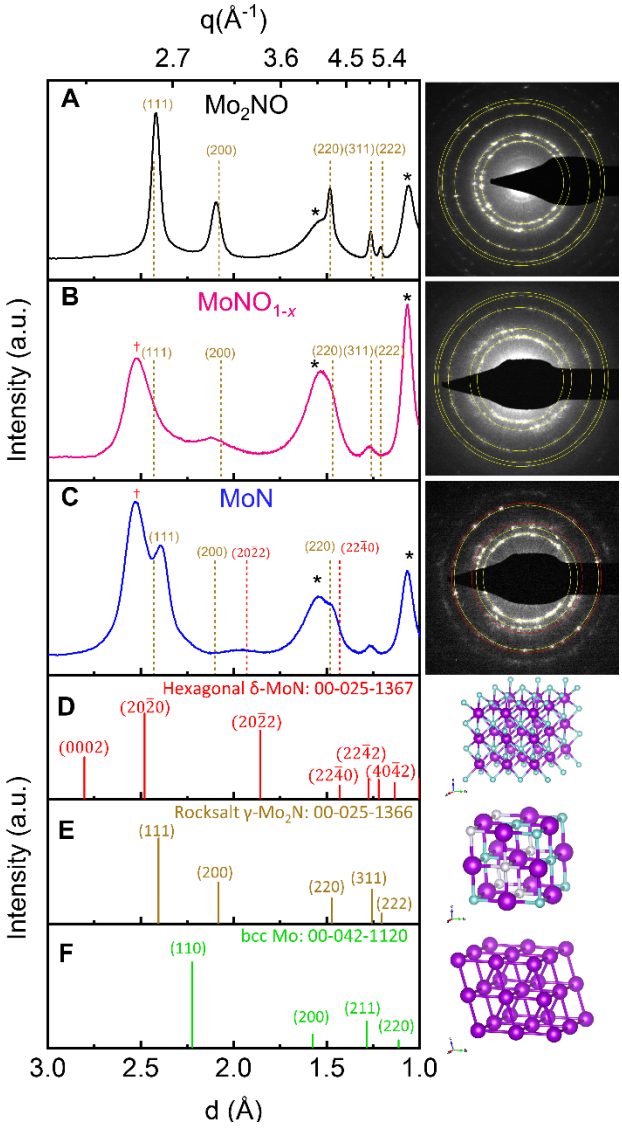

Figure 2. Structural analysis of bulk as-deposited molybdenum (oxy)nitride films. GI-XRD (th 0.5˚ on Si at 17 keV, left) and SADP (right) for (A) the predominately cubic Mo_2NO (black) and the mixed cubic-hexagonal (B) $MoNO_{1-x}$ (pink) and (C) oxygen-poor MoN (blue). Dashed lines in the GI-XRD patterns correspond to the rings in the respective SADP. Peaks and dashed lines are labeled on the diffractograms with corresponding indices. Reference patterns for (D) hexagonal δ-MoN (ICDD 00-025-1367, lattice parameters a = 5.73 Å and c = 5.61 Å, red), (E) rocksalt γ-Mo_2N structure (ICDD 00-025-1366, lattice parameter of a = 4.16 Å, yellow), and (F) bcc Mo (ICDD 00-042-1120, lattice parameter a = 3.15 Å, green) are shown below the GI-XRD with corresponding visualizations (purple = Mo, aqua = N, gray = N vacancy). Daggers denote hexagonal MoN $(20\bar{2}0)$ peaks observed by FFT and asterisks denote Si substrate peaks (Figure S6). Supporting HR-TEM, SADP, GI-XRD, and GI-XAS data can be found in Figures S4-S5 and S7-S9. Samples were in air ≤ 1 year (bulk structure is not impacted by aging, see Figure S10 for details).

The $MoNO_{1-x}$ films were synthesized at high N_2 partial pressure (6 mTorr, 100% N_2) with a substrate bias and with a high (10^{-6} Torr) base pressure (corresponding to high O content in the chamber). The GI-XRD pattern in Figure 2B shows a convolution of the hexagonal ($20\bar{2}0$) and fcc (111) peaks centered at d = 2.51 Å. Using FFT analysis, crystallites with hexagonal and rocksalt structures are observed (Figure S8). Conversely, the SADP shows only fcc structure. This difference could be due to the non-uniformity of the film, as the SADP only measures a 100 nm spot, while the GI-XRD is an average across approximately 5 - 7 cm of the sample. Using the positions of the fcc (111) and hexagonal ($20\bar{2}0$) peaks observed for MoN (Figure 2C) to deconvolute this large, broad peak centered at 2.51 Å, we can fit two peaks at 2.52 and 2.39 Å with a height ratio of 4:1 (Figure S3). From the position of the hex ($20\bar{2}0$) peak, the lattice expansion is 1.8% compared to the reference structure. Therefore, we hypothesize that the film is a mixture of hexagonal δ-MoN and fcc γ-Mo_2N. There is another possible fcc structure, B1-MoN, but because it is considered thermodynamically unstable under these synthesis conditions and is predicted to have a larger fcc lattice constant (4.20 - 4.27 Å)[49] than is observed in these films, we will refer to the fcc structure as γ-Mo_2N. A duplicate of this composition made with an increased substrate bias (-220 relative to -110 V) was found to have slight structural variations. Specifically, the film prepared with a higher substrate bias had additional diffraction peaks at 2.26, 1.55, and 1.29 Å corresponding to the (110), (200), and (211) indices of bcc Mo with a lattice parameter of 3.16 Å (Figure S3), as well as a negligible increase in bulk O content from 7.9 to 8.4%. Like the Mo_2NO film, the XANES edge is between the Mo and MoO_3 standards with no substantial pre-edge feature (Figure S4), indicating an intermediate oxidation state. The positive shift in the edge position relative to the Mo_2NO indicates that the Mo is in a higher oxidation state than it is in the Mo_2NO. The first two EXAFS coordination shells fit well using the Mo-(N/O) (2.09 Å) and Mo-Mo (2.87 Å) paths. These path lengths are similar to both the hexagonal MoN (2.15 Å and 2.86 Å, respectively) and cubic Mo_2N (2.09 Å and 2.96 Å, respectively) reference structures, meaning that the crystal structures cannot be distinguished via path length. Similar to the Mo_2NO composition, the spectrum does not fit well with a short Mo-O path characteristic of a MoO_3 structure, indicating the absence of a distinct oxide phase (Figure S8). It is notable that our fits indicate coordination numbers that are significantly lower than the crystallographic references (Mo-(N) CN = 3 for Mo_2N or 6 for MoN), however low coordination numbers have been reported for nanostructured molybdenum nitrides.[24,59]

The oxygen-poor MoN films were synthesized at high N_2 partial pressure (6 mTorr, 100% N_2) with a substrate bias and a low (10^{-7} Torr) base pressure. GI-XRD for the low substrate bias MoN is shown in Figure 2C. Diffraction peaks at 2.54 and 1.27 Å correspond to the ($20\bar{2}0$) and ($22\bar{4}2$) indices for hexagonal δ-MoN (ICDD 00-025-1367). Based on the hex ($20\bar{2}0$) peak, there is a ~2.3% lattice expansion relative to the reference structure. This magnitude of expansion is consistent with literature values for films synthesized with a high nitrogen partial pressure.[60] The peaks at 2.39 and 1.48 Å match the (111) and (220) indices of fcc γ-Mo_2N with a lattice parameter of a = 4.16 Å. HR-TEM characterization supports this mixed phase analysis, although the rings are slightly shifted from the diffraction peaks, corresponding to a mixture of a hexagonal lattice (a = 5.87 Å and c = 5.70 Å) and an fcc lattice (a = 4.19 Å). Again, the difference between the diffraction patterns observed by GI-XRD and TEM is likely due to film heterogeneity and the

small probe volume of TEM. Like the Mo_2NO and $MoNO_{1-x}$ films, the MoN duplicate had slight structural variations as a function of the substrate bias (changed from -110 to -220 V). The MoN film synthesized at higher substrate bias (220 V) differs primarily in the presence of bcc Mo metal diffraction peaks in the bulk GI-XRD, as well as a broad peak at d = 2.50 Å that can be deconvoluted into the hex $(20\bar{2}0)$ and fcc (111) peaks (Figure S3). A negligible increase in bulk O content from 3 to 4% is also observed. The XANES edge feature indicates a similar level of oxidation as the $MoNO_{1-x}$ film (Figure S4) and the first two EXAFS coordination shells can be fit with Mo-(N) and Mo-Mo paths only, indicating the absence of a separate crystalline or amorphous oxide phase like MoO_3 (Figure S9). In summary, the overall effect of synthesis conditions on bulk structure can be summarized as: high vs low N_2 pressure determines MoN vs Mo_2N structure, respectively, and at high N_2 pressures a high bias is responsible for the presence of metallic Mo within the film.

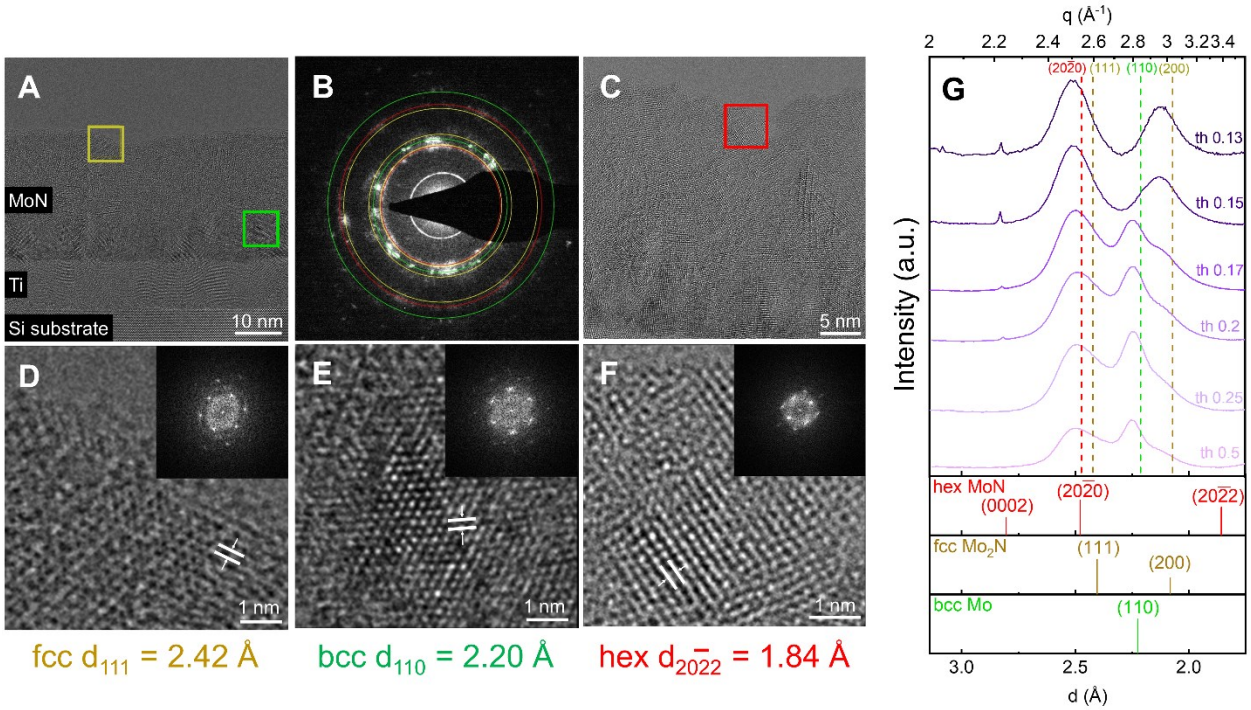

Figure 3. Characterization of an as-deposited low-oxygen high-bias (-220 V) MoN film using (A) – (F) TEM and (G) GI-XRD at different incident angles (th 0.13˚ – th 0.5˚). (A,C) Cross-sectional high resolution TEM images; (B) SADP with rings colored to match the corresponding crystal structure; (D-F) HR-TEM images corresponding to the boxed regions in (A,C), (inset) FFT analysis of the crystallites. (G) Dashed lines in the GI-XRD pattern correspond to the rings from SADP. Reference patterns for hexagonal δ-MoN (ICDD 00-025-1367, red), rocksalt γ-Mo_2N structure (ICDD 00-025-1366, yellow), and bcc Mo (ICDD 00-042-1120, green) are shown below the GI-XRD. Note: the only significant difference between this MoN sample and the one in Figure 2C is the presence of bulk Mo metal due to the high-bias synthesis. Sample was in air ≤ 1 week.

The mixed phase nature of the Mo-N thin films in this work is not unexpected based on the strong role that temperature and partial pressure (N_2 vs O_2) play in synthesis.[45,52,60,61] To better characterize the local structure and structural gradients of the synthesized films, FFT analysis and

depth-profile GI-XRD were employed. Figure 3A shows a cross-section image of the MoN film synthesized with a high substrate bias, which resulted in a mix of hexagonal δ-MoN, fcc γ-Mo_2N, and bcc Mo character (Figure S11). Using cross-sectional TEM we observe the Si substrate, ~10 nm Ti sticking layer, and Mo-N film with thickness of approximately 30 nm (Figure 3A). The SADP of the full film (Figure 3B) shows electron diffraction rings corresponding to hexagonal δ-MoN (red), fcc γ-Mo_2N (yellow), and bcc Mo (green). FFT analysis (Figure 3D-F) was used to understand the structural distribution of crystallites within the film; the regions analyzed by FFT are highlighted by colored squares in Figure 3A and C. Crystallites with fcc γ-Mo_2N (Fig 3D, yellow) and hexagonal δ-MoN (Figure 3F, red) character were identified at the surface, while a bcc Mo crystallite (Fig 3E, green) was identified at the Ti layer-film interface. These crystallites vary in size but are found to be on the order of ~ 5 nm. By probing different incident angles with GI-XRD (Figure 3G), we measured the structural depth dependence. At a probe depth of 3 - 4 nm (th = 0.13 – 0.15˚, see probe depth calculation in Figure S12),[62] two peaks were visible at d-spacings of 2.51 and 2.12 Å. The presence of these peaks at a shallow angle suggests that the surface of the film is primarily fcc γ-Mo_2N and hexagonal δ-MoN. At a depth of ~15 nm (th = 0.17˚), a third peak at 2.25 Å consistent with the (110) bcc Mo metal appears and persists into the deepest angle probed (th = 0.5˚). This result suggests that the bcc crystallites are only in the film near the substrate. Dark-field TEM imaging using the bcc Mo (110) reflection (Figure S11) supports the localization of this Mo layer to the Ti-film interface.

Collectively, the compositional (ToF-SIMS) and structural (TEM and XRD) depth profile characterization provide a more complete model of the atomic arrangements throughout the film, which allow us to construct composition-structure-activity relationships in the following sections.

2.2 Catalytic performance and selectivity evaluation of molybdenum (oxy)nitrides in acid. The catalysts were initially evaluated for the ORR by cyclic voltammetry using a rotating ring disk electrode (RRDE) in 0.1M $HClO_4$ electrolyte (Figure 4). The RRDE is used to determine the selectivity, separating the $4e^-$ (Equation 1) and $2e^-$ (Equation 2) contributions.[63] Unless otherwise stated, all catalysts were tested with less than a day of air exposure in order to minimize differences due to differential native surface oxidation. The ORR performance of each catalyst is summarized in Table S3. As per typical benchmarking protocols,[64] this voltammetric comparison provides one method for predicting how these materials could perform in a standard device. It is important to note, however, that these metrics are approximate measures of activity. To probe intrinsic activity trends, it would be necessary to normalize the amount of oxygen reduced by the number of active sites participating in ORR and the products made. This type of analysis requires an in depth understanding of the electrochemical active and available sites, which can be obscured by structural, compositional, and electronic changes during catalysis. Further discussion of intrinsic activity trends follows (see section 2.3).

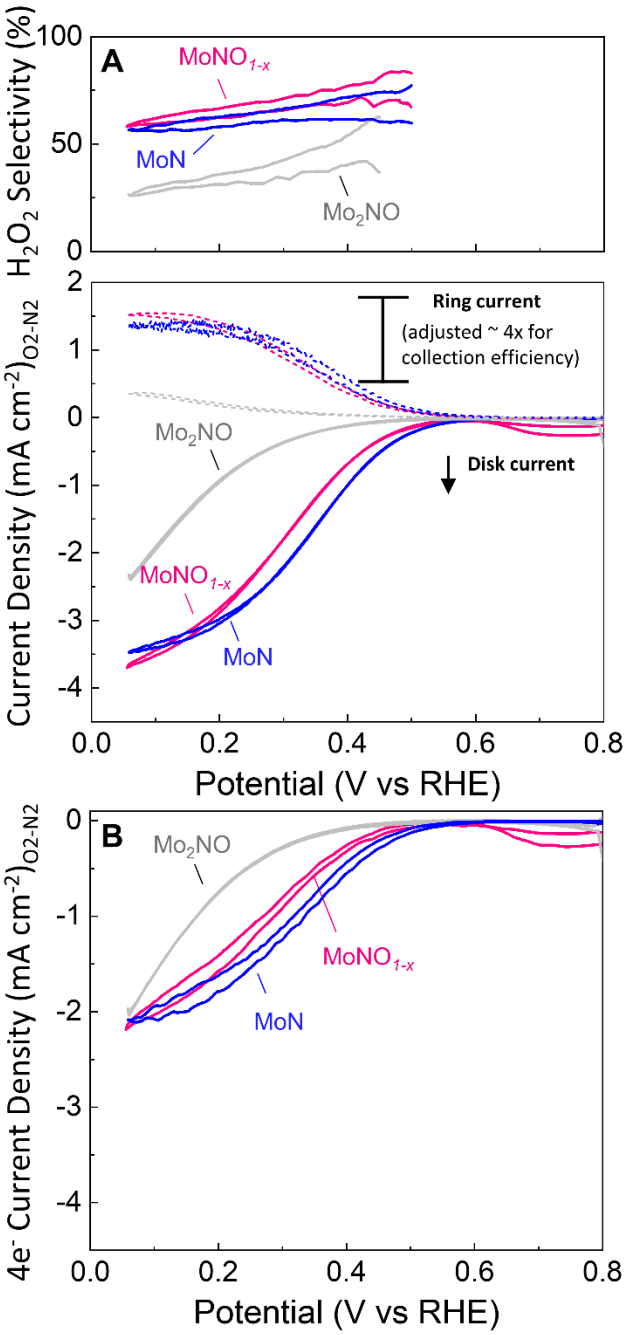

Figure 4. Cyclic voltammograms (cycle 3, 20 mV s^{-1}, 1600 rpm, O_2-saturated 0.1 M $HClO_4$) of MoN (blue), $MoNO_{1-x}$ (pink), and Mo_2NO (gray) showing **(A)** total current density (geometric basis) from the disk and the ring (Pt ring adjusted for collection efficiency, ~ 4x) and corresponding H_2O_2 selectivity, as measured by RRDE and **(B)** $4e^-$ current density (geometric).

Cyclic voltammograms (CVs), normalized by geometric surface area, are shown for representative films from the three compositions MoN, $MoNO_{1-x}$, and Mo_2NO (Figure 4); electrochemical characterization for duplicate samples can be found in the SI (Figure S13). Comparing the performance based on cyclic voltammetry, MoN shows the best ORR onset potential of 0.56 V vs

RHE at -0.1 mA cm^{-2}_{geo}, while $MoNO_{1-x}$ (x = 92%) and Mo_2NO onset at 0.52 and 0.45 V vs RHE, respectively. It is of note that these onset potentials are lower than those reported previously for Mo-N catalysts, likely due, in part, to differences in surface area, as all other reported Mo-N catalysts have been tested in nanoparticulate form with a high surface area and a conductive (carbon) support. Furthermore, the total geometric current density follows a similar trend: MoN ≥ $MoNO_{1-x}$ >> Mo_2NO. Decoupling performance trends based on selectivity, Figure 4 demonstrates that while MoN has the largest total and $4e^-$ current, $MoNO_{1-x}$ is slightly more selective for $2e^-$ ORR. The trend in H_2O_2 production, considering both selectivity and total current, is $MoNO_{1-x}$ ≥ MoN >> Mo_2NO. Although there are performance ($4e^-$ and $2e^-$) variations within each class of material, the stated trends are valid for all comparisons between the classes (Figure S13). At 0.3 V vs RHE, the $MoNO_{1-x}$ catalysts have H_2O_2 selectivities between 65 and 80% and partial H_2O_2 current densities of 0.63-0.88 mA cm^{-2}_{geo}. Comparatively, the MoN catalysts have a wider range of $2e^-$ activity, with selectivities of 21-60% and partial current densities of 0.31-0.95 mA cm^{-2}_{geo}. The higher end of this H_2O_2 production (on a geometric current density basis) is competitive with the best precious metal-free H_2O_2 catalysts in acid (Table S4).[18,65–72] Calculations of the electron transfer number using the Koutecky-Levich equation and comparison with RRDE for MoN and a poly-Pt control can be found in Figure S14.

Differences in $4e^-$ and $2e^-$ current (at all potential ranges) within each composition of catalyst indicate significant differences in intrinsic activity. However, due to the inhomogeneity of the crystallite dispersion and composition and the extreme air sensitivity of the thin films, further elucidation of the nature of the active surface is needed in order to meaningfully compare activity. Therefore, while *operando* compositional comparisons are outside of the scope of this manuscript, an electrochemical evaluation of the active surface is discussed below.

2.3 Developing activity metrics to compare dynamic heterogeneous nitride thin films. The higher activity of hexagonal δ-MoN relative to cubic γ-Mo_2N, described above, has been previously attributed to an increased Mo valence (3+ vs 1.5+) and coordination (fully coordinated octahedral without vacancies).[35] Before evaluating hypotheses for activity differences in our system, it was first necessary to determine if the observed activity trends were intrinsic catalytic effects or if they were due to other properties of the films. To isolate catalytic activity from other material properties, the film conductivity, electrochemical double layer capacitance (EDLC), and electron transfer-active surface area for each film were evaluated.

The conductivity differences between the catalysts were assessed using cyclic voltammetry of a ferrocyanide/ferricyanide redox couple.[73–75] The difference between the peak splitting values is negligible (Figure S15), but it is notable that the largest barrier to electron transfer is observed for the most active catalyst and there is no obvious correlation between peak splitting and activity. While these values are higher than the theoretical value of 59 mV, the similarity of the 3 CVs suggests that the differences in catalytic activity are not attributable to differing electronic conductivity.

Many techniques have been proposed to calculate the *active* surface area of electrodes, including *in situ* methods such as double layer capacitance measurements from voltammetry or impedance, underpotential deposition of metals, chemisorption of probe molecules or H/O, and *ex situ* methods

such as gas phase adsorption and porosimetry.[76] Since there are significant differences between the catalyst surface in air versus in electrolyte, *in situ* electrochemical methods were chosen as the most representative of the catalyst surface area under reaction conditions. The use of EDLC and the ferrocyanide/ferricyanide redox couple to determine the electrochemically active surface area(s) of the films is discussed below.

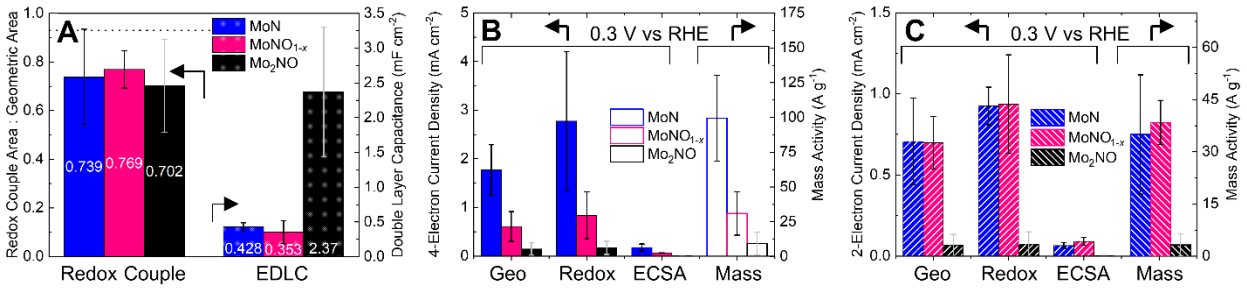

Figure 5. Calculated surface areas and ORR activity normalizations. (A) The fraction of geometric area calculated from the ferri/ferrocyanide (Fe^{2+}/Fe^{3+}) redox couple and the electrochemical double layer capacitance for the 3 catalysts. Activity for the (B) $4e^-$ and (C) $2e^-$ ORR for each catalyst normalized by geometric, redox couple, and electrochemical surface area and by total as-synthesized Mo loading in the film, as measured by ICP-OES. Error bars indicate the average of two values representing the minimum and maximum for each class of catalyst. The dashed line in (A) corresponds to the measured value for a poly-Pt film. Current densities are plotted on an absolute value basis. See Table S5 for tabulated data.

To determine the EDLC, CVs are measured in N_2-saturated electrolyte, with the scan rate varied between 20 and 200 mV/s (Figure S16).[77] Taking the slope of the current versus the scan rate, a double layer capacitance (C_{DL}, mF cm^{-2}) is calculated. An electrochemical surface area (ECSA) can be calculated using a standard reference specific capacitance (C_s) of 40 μF cm^{-2} (ECSA = $\frac{C_{DL}}{C_s}$).[78] However, because there have been no references for the C_s for TMN materials evaluated under these conditions,[79] this type of normalization may not accurately reflect the *intrinsic* ECSA. The assumption that the specific capacity is the same for all materials is complicated by the fact that the three catalysts, with nominally similar geometric surface area and total volume, have varying EDLCs, with a trend of Mo_2NO >> MoN > $MoNO_{1-x}$ (Figure 5A). It is not surprising that Mo_2NO has a significantly higher EDLC due to the extensive use of Mo_2N for supercapacitor applications.[80] Further analysis also shows that the EDLC is larger for thicker films (Figure S17). This thickness-dependent capacitance could indicate that the electrochemically available surface is deeper into the film than just the *surface* or that the thicker films are rougher (Figure S18). However, while the EDLC is unlikely to be a good metric for *intrinsic* activity in this case, we still use this as a metric of activity evaluation because it allows for a comparison between catalysts (Table S4).

For further surface area analysis, the ferri-ferrocyanide redox couple was used to determine the portion of the film that can facilitate electron transfer, a necessary condition for an ORR active site. By varying the scan rate and measuring the reduction (Fe^{3+} to Fe^{2+}) peak current, the Randles-Sevcik equation can be used to determine the area of the film that is active for electron transfer

(Figure S15, see SI for details of calculation).[81] From this calculation, it was determined that the fractions of the geometric area of the film that are conductive and participating in faradaic processes is 0.77, 0.74, and 0.70 for $MoNO_{1-x}$, MoN, and Mo_2NO, respectively (Figure 5A). Thus, both approximations of the *active* surface area show similar active areas for MoN and $MoNO_{1-x}$, while Mo_2NO has a much higher capacitance.

Normalizations of the $2e^-$ and $4e^-$ ORR current density at 0.3 V vs RHE by the *electrochemically active* surface areas and the Mo loading (total Mo mass, as determined by ICP-OES) allows for further analysis of the intrinsic activity of the three catalyst types (Figure 5B-C). Critically, the $4e^-$ activity trend is $MoN \geq MoNO_{1-x} >> Mo_2NO$, regardless of the normalization used. The $2e^-$ activity trend shows more variation, with MoN and $MoNO_{1-x}$ producing similar current densities by all normalization metrics, while Mo_2NO is a poor catalyst by all metrics. Normalization of the CVs by these metrics also shows that onset potential and saturation current density trends do not change (Figure S19), suggesting that the observed activity differences are intrinsic to the catalyst and not merely due to differences in quantity of active sites. Further discussion of these intrinsic differences can be found in the next section.

It is important to note that the maximum current, or mass transport (MT) limited current, observed in the CVs is lower than would be predicted by the Levich equation based on the calculated electron transfer number by either the RRDE or Koutecky-Levich methods (Figure S14). This phenomenon is frequently observed for non-precious metal ORR catalysts[27,28,34,38] and could be attributed to a number of factors including: low density of active sites, electronically-disconnected regions, *in situ* catalyst changes, and parasitic reactions.

2.4 Experimental and theoretical evaluation of the impact and incorporation of oxygen. In the previous sections, we have determined that there are structural and compositional differences, and corresponding intrinsic activity differences, between the three categories of catalysts. Herein we discuss the role of crystal structure and composition in ORR activity and provide a theoretical framework for understanding the role of N vacancies and O substitution in the stability of nitride structures and their activity for the ORR.

2.4.1 Bulk oxygen correlation with $4e^-$ ORR activity. As shown previously, regardless of the active site normalization technique, the $4e^-$ ORR activity trend is $MoN \geq MoNO_{1-x} >> Mo_2NO$ (Figure 5B). We therefore utilized our extensive materials characterization of these catalysts to understand the effect of specific material properties on the intrinsic activity. Figure 6 shows the geometric current density at 0.3 V vs RHE for the 6 catalysts (3 classes, each with a duplicate) versus the bulk (A) rocksalt: hexagonal (fcc: hex) structural ratios, (B) N content, and (C,D) O content. It should be noted that the fcc: hex ratio is a qualitative approximation for structural content, since quantification is complicated by the varying sizes of crystallites. From these plots, we can identify that the catalysts with the highest current density (and thus the highest ORR activity) have mixed hexagonal-cubic structures, high N content, and low O content.

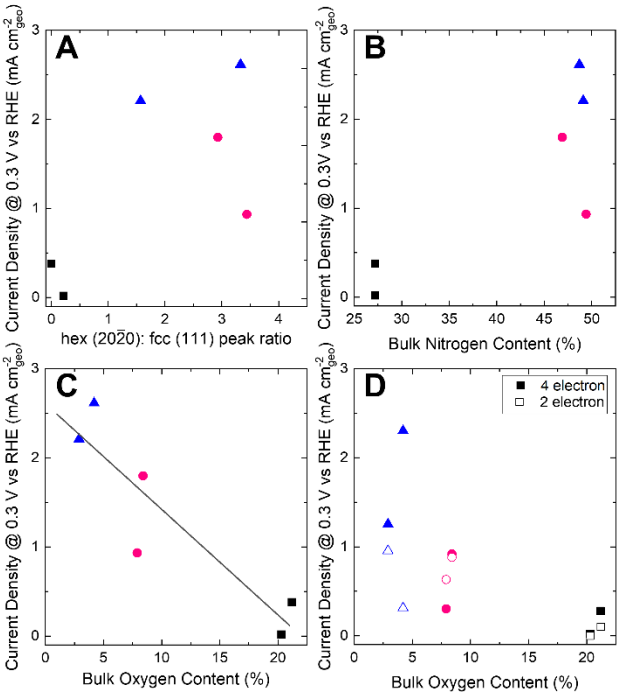

Figure 6. Comparison of activity with structure and composition. Absolute value of the geometric current density at 0.3 V vs RHE versus (A) the height ratio of the hexagonal (20$\bar{2}$0) and fcc (111) peaks, (B) the bulk N content, and the bulk O content for (C) total current density and (D) 2e$^-$ and 4e$^-$ current density in the films for Mo_2NO (black, squares), MoN (blue, triangles), and $MoNO_{1-x}$ (pink, circles). The two points for each color correspond to the 2 duplicates for each class of catalyst.

Although it would be most informative to understand the role of each property individually, it is difficult to decouple the effects of N:Mo ratio and structure, since composition is not independent of structure. For example, while there is a difference in structure between Mo metal (bcc) and Mo-N (fcc or hex) and thus the effect of N cannot be fully isolated from that of structure, we do note that Mo metal shows no ORR activity (Figure S20), suggesting that N is important for activity. Significantly, we demonstrate that at the same N:Mo ratio, bulk O content (Figure 6C) correlates with the observed activity differences between the mixed hexagonal-cubic structures. This strong correlation was unexpected, as the role of O content in (pure) nitride catalysts has not been well-explored. Structural strain in the films does correlate weakly with this O content, with the high O content rocksalt Mo_2NO showing the highest fcc lattice constant (Figure S21), but otherwise the effect of the O content on the nitride structures is non-obvious. Interestingly, we show that 2e$^-$ ORR current (at 0.3 V vs RHE) is relatively insensitive to bulk O content, whereas 4e$^-$ ORR current has a strong O dependence (Figure 6D). This result suggests that selectivity can be tuned by decreasing bulk O content and therefore increasing 4e$^-$ activity.

2.4.2 Theoretical discussion of O incorporation. Given the observed correlation between bulk O content and ORR activity, it is important to understand the thermodynamics of O incorporation into the Mo-N structures, as well as the favorable sites for O substitution or incorporation. Using DFT, we computed the theoretical energy of O substitution within the cubic and hexagonal Mo-N

structures with varying vacancy and O concentrations. Computational details are provided in the experimental section. Equation 3 represents the O substitution equation under ambient conditions. The energy of the reaction, represented by ΔG_O^{sub}, was computed via DFT for each structure.

$$MoN_n + ½\ O_2 \rightarrow MoN_nO \qquad [3]$$

To probe the role of O in the lattice, we considered O:Mo ratios from 0 – 0.5 within the N-vacancy containing Mo-N structures. Figure 7B shows the predicted ΔG_O^{sub} for each composition that was considered. The results indicate that O substitution is thermodynamically favorable for nearly all of the structures under ambient conditions.

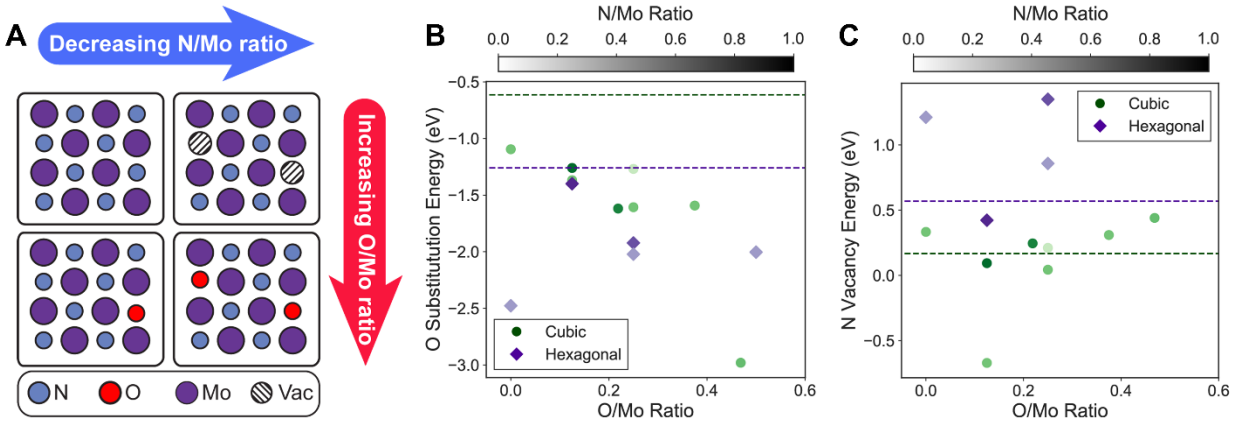

Figure 7. (A) A schematic indicating how N/Mo and O/Mo ratios relate to the atomic structures being modeled. An increasing O/Mo ratio corresponds to O substitution, while a decreasing N/Mo ratio is the result of O substitution or N vacancies. (B) Predicted ΔG_O^{sub} under ambient conditions and (C) predicted nitrogen vacancy formation energies in Mo-N under ambient conditions at varying O/Mo and N/Mo ratios. The diamonds and circles indicate hexagonal and cubic Mo-N, respectively. The color of each point relates to the N/Mo ratio; lower N/Mo ratios indicate higher N vacancies. The purple and green dashed lines indicate the substitution energy for the ideal hexagonal and cubic structures, respectively.

To explore the sensitivity of ΔG_O^{sub} to the configuration of N vacancies and O defects, we computed ΔG_O^{sub} for 30 structures of randomly selected N vacancy sites at four different O concentrations at a 2:1 ratio of Mo:N. These computations yielded up to 0.25 eV standard deviation in O substitution energies for these structures. The O substitution energies of all the Mo-N structures containing defects fall below that of the respective ideal cubic and hexagonal structures. Collectively, the results indicate that both O substitution and N vacancy formation reduce ΔG_O^{sub}. This trend may arise from increased distortion within the cubic and hexagonal lattices at large defect concentrations.

ΔG_O^{sub} is a purely thermodynamic quantity and will only determine the incorporation of O into MoN films if the kinetics are facile. Diffusion through bulk nitride phases can be kinetically prohibitive, as is the case for barrier materials such as TiN. However, crystal defects such as vacancies and grain boundaries have been shown to greatly reduce the diffusion barriers of nitrogen and O in transition metal nitrides.[82] The high vacancy concentration and polycrystalline

nature of the Mo-N films, particularly in the cubic structures, will result in higher O diffusivity, which reduces kinetic diffusion barriers and causes thermodynamics to govern O incorporation. The significant incorporation and distribution of O into the Mo-N structures, without formation of regions of MoO_x, in the films during synthesis indicates that O diffusion kinetics are facile.

The nitrogen vacancy defects may also be used to understand differences in O incorporation. As vacancies facilitate O diffusion in Mo-N films, a material may be resistant to O incorporation due to a high nitrogen vacancy formation energy. Figure 7C shows the relative nitrogen vacancy formation energies for both ideal and defective Mo-N in the cubic and hexagonal structures. Nearly all the cubic Mo-N structures have a lower vacancy formation energy than hexagonal Mo-N. This may explain the relatively low amount of O and vacancy concentrations found in hexagonal Mo-N films above. Without a significant concentration of vacancy sites to host O defects, the O content in hexagonal Mo-N films will be limited.

The correlation between bulk O content in the Mo-N structures and ORR activity provides a guideline for synthesizing active Mo-N-based catalysts. However, it is unlikely that bulk O content is the direct cause of the difference in ORR activity between different Mo-N films. While surface O content is more likely to describe the differences in activity of Mo-N films than bulk O content, *ex situ* air contamination makes direct measurement of the composition of the active surface difficult. However, as shown in Figure 7C, the cubic Mo-N structure has a greater driving force for N vacancy formation compared to the hexagonal structure, and these vacancies correspond to more facile O incorporation. As a result, structures with a greater proportion of cubic crystallites will have a larger oxygen content. We have shown that the different crystallite phases in the bulk of the films interact with O differently, which likely corresponds to differences in the ability of crystallite phases at the surface to bind ORR intermediates. This may explain the observed correlation between bulk O content and ORR activity.

The significant number of N vacancies and O substitution defects within each Mo-N structure coupled with the potential evolution of Mo-N surfaces during ORR results in an intractable number of possible active site motifs. This complexity poses a significant challenge to theoretical modeling of the relevant surface under reaction conditions. It will be imperative for future studies to address the complexity of this active surface phase in order to fully elucidate the role of surface O substitution in ORR activity.

2.5 Electrochemical and material stability. In addition to determining the relationship between activity and composition, it is important to understand the limits of material stability during catalysis. We evaluated the stability of the Mo-N catalysts using 5 and 25 h chronoamperometry (polarization) tests and characterized changes in their material properties using *ex situ* ICP, XPS, GI-XRD, and TEM (Figure 8).

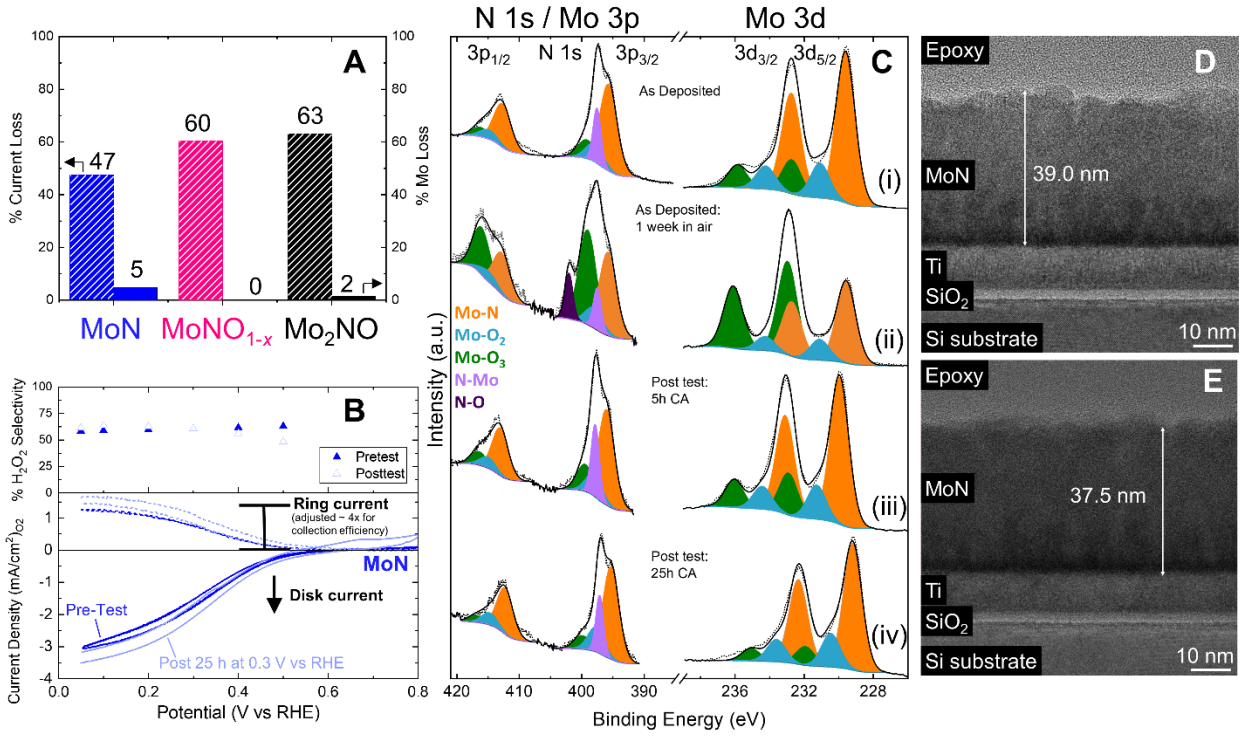

Figure 8. Stability measurements showing (A) the change in current density and Mo content, as determined by ICP-OES, after 5 h polarization at 0.3 V vs RHE for MoN (blue), $MoNO_{1-x}$ (pink), and Mo_2NO (black) on doped-Si substrates. (B) CVs of MoN before and after a 25 h polarization at 0.3 V vs RHE using a rotating ring disk electrode (Pt ring) showing disk current, ring (adjusted for collection efficiency) current, and calculated H_2O_2 selectivity. (C) Mo 3d and Mo3p/N1s XPS spectra for the MoN film (i) immediately after deposition, (ii) after 1 week in air, and after polarization at 0.3 V vs RHE for (iii) 5 h and (iv) 25 h. HR-TEM of a MoN film on a doped-Si substrate (D) before and (E) after a 25 h polarization at 0.3 V vs RHE. All electrochemical measurements were done in O_2-saturated 0.1 M $HClO_4$ with 1600 rpm rotation.

The exact composition of many transition metal compounds (nitride, oxide, carbide, sulfide etc.) during electrochemical analysis in aqueous media is highly contested due to their potential-dependent conversion to oxides/(oxy)hydroxides (at more positive potentials) or metals (at more negative potentials).[83,84] Due to this known complication, it is particularly important to characterize the bulk and surface composition. It is of note that even prior to electrochemical analysis, the as-deposited films are substantially (> 20 %) oxidized, as seen by both ToF-SIMS (Figure 1 and Figure S2) and XPS (Figure S22, Table S6). Despite this high level of oxidation, N is also visible on the surface suggesting an oxynitride surface layer for all the films tested. It is important to emphasize that the Mo $3p_{3/2}$ and N 1s regions overlap significantly, and that it is non-trivial and imperative to deconvolute the two components (please see Figure S22, Table S6, and the subsequent fitting explanation). Using the MoN catalyst as an example, XPS shows that the level of oxidation (in the top ~ 6 nm) increases in ambient conditions and after ~ 1 week in air the surface O content (based on the MoO_2 and MoO_3 components) rises from 30% (1 day) to 50% (1 week, Figure 8C). Similarly, in the N 1s spectrum (see the SI for details of the deconvolution of

Mo 3p and N1s spectra), the metal nitride peak at 397.6 eV at day 1 is joined by a N-O peak at 402.1 eV after 1 week. Although the effect of air exposure on ORR activity or selectivity is unclear, there is an increase in EDLC with time in air (Figure S23). Therefore, all catalysts are stored under Ar in a glovebox to prevent further oxidation and allow for accurate comparison between samples.

While this extreme air sensitivity makes it complicated to confidently compare *ex situ* surface O compositions as a function of reaction time, it is still possible to monitor the Mo and N stability. Using ICP-OES to probe the film mass after a 5 h polarization at 0.3 V vs RHE (Figure 8A), we see < 5 % loss of Mo for all compositions. However, the catalysts lose 50 – 65 % of their catalytic activity during the 5 h polarization (Figure S24). This loss of ORR activity without substantial Mo loss suggests that being held at a relatively reducing potential is decreasing the intrinsic activity of the catalyst or the density of active sites.

To evaluate longer-term stability, the most promising composition, MoN, was tested via polarization at 0.3 V vs RHE for 25 h. During this stability evaluation, periodic ICP-MS aliquots of the electrolyte (Figure S25) indicate the majority (6 - 9 %) of mass loss (Mo dissolution) happens during the cyclic voltammetry before and after the 25 h polarization. During the polarization itself, only ~ 3 % Mo dissolution is measured. HR-TEM (Figure 8D and E) supports this high material stability, with less than 2 nm of film thickness lost after the long-term polarization. Additionally, elemental mapping shows no change in bulk N after polarization, indicating bulk nitride stability (Figure S26). Catalytically, however, over the course of 25 h at 0.3 V vs RHE there is a ~ 55 % decrease in current density. Like the 5 h polarization, ~ 35 % of the total performance loss happens in the first hour. It is notable that the activity lost during the polarization is recoverable (Figure 8B), with the post-test CV showing small improvements in onset potential and mass transport limited current density. Taken together, these experiments indicate that the catalyst is electrochemically but not chemically stable during CVs, while the reverse is true during a polarization at 0.3 V vs RHE. We hypothesize that the film forms a less active surface while held at this reducing potential that is removed after cycling, resulting in an observed loss of material and restoration of activity. Based on *ex situ* XPS of MoN (Figure 8C) the Mo-N content on the surface does not change during catalysis, with the post test samples (iii, iv) showing compositions very similar to the as-deposited films (i). As shown by GI-XRD at th 0.13˚ (probing ~ 2 nm into the surface), after catalysis there is little to no shift in the hexagonal ($20\bar{2}0$) peak (Figure S27). A peak shift would have been consistent with an increasing lattice expansion with decreasing O content.[58]

Overall, we conclude that the films lose significant electrochemical activity during polarization stability tests, but that much of this activity is recoverable via cycling. We further find that the bulk structure and morphology are stable under the reaction conditions studied, while small structural and substantial composition changes are observed at the surface.

3.0 Conclusion

Three compositions of carbon-free, molybdenum (oxy)nitride thin film catalysts have been investigated as catalysts for the ORR. Extensive characterization of the catalyst surface and bulk demonstrated the heterogeneity throughout the film and the local crystalline order, as well as the

significant O content in the bulk and on the surface of the films. DFT calculations revealed the thermodynamic favorability of bulk oxynitride formation, with a strong driving force for O incorporation into the defected rocksalt Mo_2N structure with a high concentration of N vacancies. Bulk structure and composition, particularly O content, were found to influence the interactions of the films with O and correlate with electrochemical performance. Maximal ORR activity was achieved through minimization of bulk O content in a mixed hexagonal-cubic film with a high N:Mo ratio. Much higher H_2O_2 selectivity, 20 – 60%, was found than had previously been reported for Mo-N catalysts. The compositional changes to the surface observed by *ex situ* characterization as a function of air exposure motivate further *in situ* investigations of the role of O, N vacancies, and Mo oxidation state in determining ORR activity and selectivity. The composition-based activity trends, high material stability, and recoverable electrochemical performance highlight the importance of deconvoluting chemical and catalytic performance and inform possible routes towards activity and stability enhancement.

4.0 Experimental

4.1 Materials. Glassy carbon electrodes (Pine Research Instrument, 0.196 cm^2 geometrical area), graphite counter electrode, Ag/AgCl reference electrode (Fisherbrand, Accumet), silicon wafers (WRS, 100 mm, P/Bor <100>, 10-20 Ohm-cm), Mo sputtering target (Kurt J Lesker, 99.99% purity, 2" diameter), Ti sputtering target (Kurt J Lesker, 99.99% purity, 2" diameter), and perchloric acid (Honeywell Fluka, 70%), were all used as received and without further purification unless otherwise stated.

4.2 Synthesis. Molybdenum nitride thin films were prepared by DC reactive sputtering using a Lesker Sputter. Prior to the nitride synthesis, a 10 nm thick Ti sticking layer was sputtered (2 minutes, 200W, 100% Ar, 3 mTorr) onto the polished glassy carbon disk electrode. Subsequently, without breaking vacuum, the Mo target was sputtered in pure Ar for 1 minute (to avoid nitridation of the Ti sticking layer) and then in a mixture of Ar and N_2 plasma to deposit ~30 nm of Mo-N. The magnetron power supply was maintained at 200 W and the chamber pressure was 6 mTorr. The substrate was held at 180 ± 10 ˚C with a substrate bias of (-) 0-220 V throughout the deposition. Films were also synthesized on Si wafers, with the native SiO_2 layer chemically (HF) or physically (2 min sputter etch in sputtering chamber under vacuum) etched, for structural and electrochemical characterization. The chemical HF etch used the following common cleaning procedure. The wafers were initially cleaned with a SC1 etch (5:1:1 $H_2O/H_2O_2/NH_4OH$ at 50 °C for 10 min), followed by a SC2 etch (H_2O/H_2O_2/HCl at 50 °C for 10 min) and concluded with a 30 s HF etch. See Table 1 for synthetic details for each film.

4.3 Physical characterization. GI-XRD was performed at beamline 2-1 at the Stanford Synchrotron Radiation Lightsource (SSRL) at SLAC National Laboratory using 17 keV radiation. The incident energy was selected using a Si(111) monochromator. A Pilatus 100K was mounted ~700mm from the sample. A pair of Soller slits were placed between the sample and the detector (~100 mm from the sample). Grazing incidence angles of 0.13-0.5˚ were chosen to probe the full depth of the film. 500 detector images were collected for each incidence angle to cover a 2-theta range of 12-44˚ in 0.08˚ increments. The 2D Pilatus images were converted to k-space and integrated to produce the plots shown in this paper. The integrated data was smoothed using a

Savitzky-Golay filter and the background was subtracted. The data was processed using a refraction correction to account for differential refraction of incident X-rays at different grazing incidence angles. Details of this correction are provided in the SI.[85] Lab scale GI-XRD was performed using a D8 Venture single crystal diffractometer (Bruker, λ=1.5418 Å) at an incidence angle of 5˚.

X-ray photoelectron spectroscopy (XPS) was performed with a Phi Versaprobe 3 using monochromatized Al Kα (1486 eV) radiation. All XPS spectra were calibrated to the C 1s peak at a binding energy of 284.8 eV. CasaXPS software was used to perform peak fitting with Shirley backgrounds and Gaussian-Lorentzian lineshapes. Details of the fitting procedure and statistics for the fits are included in the SI.

Mo K-edge grazing incidence X-ray absorption spectroscopy (XAS) measurements were conducted at beamline 11-2 at SSRL. Energy resolved fluorescence signal for XAS was collected with a monolithic 100-element Canberra germanium detector mounted at a 90° angle to the incident beam with the ROI set on the Mo K-alpha feature. Photon energy was resolved and integrated with XIA DXP-XMAP digital photon processors. A Pilatus 100K area detector was used to measure scattered X-ray intensity. Harmonics were eliminated using a Rh coated silicon collimating mirror with a cutoff set at ~ 21.5 keV. The beam was focused to approximately 30 μm using a silicon toroidal mirror after the monochromator. The incident energy was selected using a liquid N_2 cooled double crystal monochromator with Si(220) phi = 90 crystal cut. Energy was calibrated with a Mo metal foil collected simultaneously with each data sweep and the maximum of the first feature in the first derivative was assigned as 20 keV. A shallow incidence angle of 5˚ was chosen to probe the bulk of the film and increase the signal. XAS spectra were normalized using the background subtraction and intensity normalization functions in the Athena software package.[86] Fourier transform parameters were k-range = 3-11.1 with a Hanning window. Averages of two sequential spectra were used to increase the signal-to-noise ratio. EXAFS data was fit in R-space using multiple k-weight (k=1,2,3) co-refinement in the Artemis software package and cif files from the Inorganic Crystal Structure Database.[87] A value of 0.8 was used for S_o^2 based on fitting of a Mo standard (Figure S28). Further details for the fits are provided in the SI. In the grazing incidence geometry, self-absorption can complicate analysis of peak intensities in XANES and coordination number in EXAFS. However, at the incidence angle of 5˚ and energy of 20 keV, the attenuation length in the film is approximately 1.34 μm (~45x the film thickness). Therefore, the entire thickness of the film is being probed and self-absorption effects are minimal for this experiment.

ToF-SIMS studies were carried out at the Center for Nanophase Materials Sciences (CNMS) at Oak Ridge National Laboratory using the ToF.SIMS.5 NSC instrument (ION.TOF Gmb). A Bi_3^+ liquid metal ion gun (30 keV energy, 30 nA current and 5 mm spot size) was used as the primary ion beam for secondary ions extraction from the surface of the sample. Secondary ions were further analyzed using a time-of-flight mass analyzer in positive ion detection mode with mass resolution $m/\Delta m$ = 3,000 – 10,000. A Cs^+ ion beam (1 keV energy, 70 nA current and 15 μm spot size) was used as a sputter source for depth profiling. Measurements were performed in non-interlaced mode, where each scan by the Bi_3^+ primary beam (50 x 50 μm^2) was followed by 5 s of sputtering with

the Cs^+ (300 x 300 μm^2). Atomic Force Microscopy measurements of sputtered craters were further used for calibration of the depth profiles. $CsMo^+$, Cs_2O^+, CsN^+ and $CsTi^+$ clusters were used to track concentrations of Mo^+, O^-, N^- and Ti^+ respectively. Data was analyzed with the SurfaceLab 7.0 (ION.TOF Gmb) software.

Conventional cross-sectional TEM specimens were prepared to study the morphology and structure of the thin film.[88] The samples were glued using epoxy to form a sandwich structure, cut, and mechanically polished to 15 μm in thickness. The specimen was further milled by an Ar^+ ion beam to create electron transparent region in a Gatan PIPS II ion milling machine. The Ar^+ ion beam was first induced with 5 keV energy at 5-degree incident angle and gradually reduced to 0.5 keV for final cleaning. HR-TEM images and SADP were taken in a FEI Titan Environment TEM with an image corrector operated at 300kV. The HR-TEM images and SADPs were calibrated using the lattice and diffraction pattern of the Si substrate as reference. The Oxford Xmax SDD Detector was used for energy-dispersive X-ray spectroscopy (EDS) analysis. Scanning TEM annular dark field (STEM-ADF) images and EDS mappings were taken with a probe size of 0.3 nm. The STEM-ADF images were taken with convergence angles of 18.6-25.4 mrad.

4.4 Electrochemical Testing. Electrochemistry was performed using a rotating disk electrode (Pine Research Instrument) in a three-electrode glass cell, with 0.1 M $HClO_4$ electrolyte purged with oxygen or nitrogen. A Ag/AgCl electrode (accumet) was used as the reference electrode and a graphite rod as the counter electrode. Reference electrodes were calibrated for each batch of electrolyte using a standard hydrogen electrode (hydrogen bubbling over a flame annealed Pt coil).[89] The series resistance of the cell was measured at 100 kHz and the iR losses were compensated at 85%. Electrochemical activity was assessed using cyclic voltammetry, sweeping reversibly from 0.8 V to 0.05 V at a scan rate of 20 mV/s using a Biologic VSP-300 Potentiostat. Unless otherwise stated, the oxygen purged voltammograms were corrected for background current by subtracting the baseline (nitrogen) sweep. Stability was evaluated using chronoamperometry. Selectivity measurements were conducted using a rotating ring disk electrode (Pine Research Instrument) with a Pt ring held at 1.2 V vs RHE to measure the H_2O_2 produced in the reaction. The ring was calibrated periodically using a standard ferri/ferrocyanide couple.[63] See the SI for details of selectivity calculations (Figure S14). Double layer capacitance was measured by taking CVs in N_2 saturated electrolyte at different scan rates. Ferro/ferricyanide redox experiments were conducted in N_2 saturated 1 M KNO_3 supporting electrolyte with 10 mM potassium ferricyanide with CVs at varying scan and rotation rates. Activity and selectivity measurements were performed using a polished GC disk working electrode (SIGRADUR G). However, the GC disks were unsuitable for structural measurements via GI-XRD due to the high background signal from the carbon (Figure S29). All electrochemical measurements done on a doped-Si substrate, for the purpose of subsequent structural characterization, were performed by adhering the doped wafer onto the surface of a GC electrode using a GaIn eutectic and carbon paste. The GC:Si sample was glued onto the disk insert holder (Pine Research) using an epoxy and dried prior to testing and rotation. All measurements on doped-Si samples were normalized to the measured surface area of the doped-Si sample. It is difficult to compare the electrochemistry of one sample on a GC disk and Si wafer directly due to differences in conductivity, geometry of the electrodes, and hydrodynamics of the rotating disk electrode vs rotating Si piece, but the analogous

activity trends between samples indicate that the oxynitride films respond similarly regardless of substrate (Figure S24).

4.5 Computational Details. The formation energy of oxygen vacancies were computed using DFT as implemented in the Vienna Ab initio Simulation Package (VASP).[90] Mo-N structures were simulated using the RPBE functional with a 500 eV plane wave cut-off and projector augmented wave method (PAW) pseudopotentials.[91,92] A 5x5x5 k-point mesh was used to simulate bulk Mo-N structures, and unit cell dimensions were allowed to relax to optimize the lattice parameters at varying vacancy and oxygen substitution concentrations. A force convergence criterion of 0.005 eV/Å was used for structure optimization.

Description of Supporting Information

Additional materials characterization (ToF-SIMS, GI-XRD, TEM, GI-XAS, XPS), electrochemical measurements and calculations, correlations between structure, composition, and activity, theoretical structures and details, and post-test characterization.

Acknowledgements

The authors gratefully acknowledge the support of the Toyota Research Institute. The U.S. Department of Energy (DoE) Office of Basic Energy Sciences (BES) is gratefully acknowledged for primary support for SUNCAT Center for Interface Science and Catalysis. Part of this work was performed at the Stanford Nano Shared Facilities (SNSF) and the Stanford Nanofabrication Facility (SNF), supported by the National Science Foundation under Award ECCS-1542152. Use of the Stanford Synchrotron Radiation Lightsource, SLAC National Accelerator Laboratory, is supported by the U.S. DoE, Office of BES under Contract No. DE-AC02-76SF00515. Part of this research (ToF-SIMS characterization) was conducted at the Center for Nanophase Materials Sciences, which is a DOE Office of Science User Facility, using instrumentation within ORNL's Materials Characterization Core provided by UT-Battelle, LLC under Contract No. DE-AC05-00OR22725 with the U.S. DoE. The authors thank Guanchao Li in the Stanford Environmental Measurements Facility for the acquisition of ICP-MS and OES data. The authors thank Kevin Stone for the XRD integration code. Authors MEK and MBS would like to thank Chris Hahn and Alan Landers for insightful discussions. Author AP thanks the National Science Foundation Graduate Research Fellowship Program (NSF GRFP).

References

(1) Crabtree, G. W.; Dresselhaus, M. S.; Buchanan, M. V. The Hydrogen Economy. *Phys. Today* **2004**, *57* (12), 39–45.

(2) Evans, A.; Strezov, V.; Evans, T. J. Assessment of Utility Energy Storage Options for Increased Renewable Energy Penetration. *Renew. Sustain. Energy Rev.* **2012**, *16*, 4141–4147.

(3) Technology Roadmap: Hydrogen and Fuel Cells, 2015. International Energy Agency. http://ieahydrogen.org (accessed Feb 20, 2020).

(4) Ball, M.; Weeda, M. The Hydrogen Economy - Vision or Reality? *Int. J. Hydrogen Energy* **2015**, *40*, 7903–7919.

(5) Wang, C.; Yu, Y.; Niu, J.; Liu, Y.; Bridges, D.; Liu, X.; Pooran, J.; Zhang, Y.; Hu, A. Recent Progress of Metal-Air Batteries - A Mini Review. *Appl. Sci.* **2019**, *9*, 2787.

(6) Rahman, M. A.; Wang, X.; Wen, C. High Energy Density Metal-Air Batteries: A Review. *J. Electrochem. Soc.* **2013**, *160* (10), A1759–A1771.

(7) Chang, Z.; Zhang, X. Introduction to Metal-Air Batteries: Theory and Basic Principles. In *Metal–Air Batteries: Fundamentals and Applications*; Wiley-VCH: Chennai, 2018; pp 1–9.

(8) Li, Y.; Lu, J. Metal−Air Batteries: Will They Be the Future Electrochemical Energy Storage Device of Choice? *ACS Energy Lett.* **2017**, *2*, 1370–1377.

(9) Gasteiger, H. A.; Kocha, S. S.; Sompalli, B.; Wagner, F. T. Activity Benchmarks and Requirements for Pt, Pt-Alloy, and Non-Pt Oxygen Reduction Catalysts for PEMFCs. *Appl. Catal. B Environ.* **2005**, *56*, 9–35.

(10) Sharma, M.; Jung, N.; Yoo, S. J. Toward High-Performance Pt-Based Nanocatalysts for

Oxygen Reduction Reaction through Organic−Inorganic Hybrid Concepts. *Chem. Mater.* **2018**, *30*, 2–24.

(11) Stamenkovic, V. R.; Mun, B. S.; Arenz, M.; Mayrhofer, K. J. J.; Lucas, C. A.; Wang, G.; Ross, P. N.; Markovic, N. M. Trends in Electrocatalysis on Extended and Nanoscale Pt-Bimetallic Alloy Surfaces. *Nat. Mater.* **2007**, *6*, 241–247.

(12) Wang, L.; Holewinski, A.; Wang, C. Prospects of Platinum-Based Nanostructures for the Electrocatalytic Reduction of Oxygen. *ACS Catal.* **2018**, *8* (10), 9388–9398.

(13) Wagner, F. T.; Lakshmanan, B.; Mathias, M. F. Electrochemistry and the Future of the Automobile. *J. Phys. Chem. Lett.* **2010**, *1*, 2204–2219.

(14) Kongkanand, A.; Mathias, M. F. The Priority and Challenge of High-Power Performance of Low- Platinum Proton-Exchange Membrane Fuel Cells. *J. Phys. Chem. Lett.* **2016**, *7*, 1127–1137.

(15) Bashyam, R.; Zelenay, P. A Class of Non-Precious Metal Composite Catalysts for Fuel Cells. *Nature* **2006**, *443*, 63–66.

(16) Yang, S.; Verdaguer-Casadevall, A.; Arnarson, L.; Silvioli, L.; Čolić, V.; Frydendal, R.; Rossmeisl, J.; Chorkendorff, I.; Stephens, I. E. L. Toward the Decentralized Electrochemical Production of H2O2: A Focus on the Catalysis. *ACS Catal.* **2018**, *8*, 4064–4081.

(17) Crole, D. A.; Freakley, S. J.; Edwards, J. K.; Hutchings, G. J. Direct Synthesis of Hydrogen Peroxide in Water at Ambient Temperature. *Proc. R. Soc. A* **2016**, *472*, 1–9.

(18) Siahrostami, S.; Verdaguer-Casadevall, A.; Karamad, M.; Deiana, D.; Malacrida, P.; Wickman, B.; Escudero-Escribano, M.; Paoli, E. A.; Frydendal, R.; Hansen, T. W.; et al. Enabling Direct H2O2 Production through Rational Electrocatalyst Design. *Nat. Mater.*

2013, *12*, 1137–1143.

(19) Chen, S.; Chen, Z.; Siahrostami, S.; Higgins, D.; Nordlund, D.; Sokaras, D.; Kim, T. R.; Liu, Y.; Yan, X.; Nilsson, E.; et al. Designing Boron Nitride Islands in Carbon Materials for Efficient Electrochemical Synthesis of Hydrogen Peroxide. *J. Am. Chem. Soc.* **2018**, *140* (25), 7851–7859.

(20) Wu, G.; More, K. L.; Johnston, C. M.; Zelenay, P. High-Performance Electrocatalysts for Oxygen Reduction Derived from Polyaniline, Iron, and Cobalt. *Science.* **2011**, *332*, 443–447.

(21) Lefèvre, M.; Proietti, E.; Jaouen, F.; Dodelet, J. P. Iron-Based Catalysts with Improved Oxygen Reduction Activity in Polymer Electrolyte Fuel Cells. *Science.* **2009**, *324*, 71–74.

(22) Artyushkova, K.; Workman, M. J.; Matanovic, I.; Dzara, M. J.; Ngo, C.; Pylypenko, S.; Serov, A.; Atanassov, P. Role of Surface Chemistry on Catalyst/Ionomer Interactions for Transition Metal–Nitrogen–Carbon Electrocatalysts. *ACS Appl. Energy Mater.* **2018**, *1*, 68–77.

(23) Jiang, W.-J.; Gu, L.; Li, L.; Zhang, Y.; Zhang, X.; Zhang, L.-J.; Wang, J.-Q.; Hu, J.; Wei, Z.; Wan, L. Understanding the High Activity of Fe−N−C Electrocatalysts in Oxygen Reduction: Fe/Fe3C Nanoparticles Boost the Activity of Fe−Nx. *J. Am. Chem. Soc.* **2016**, *138*, 3570–3578.

(24) Morozan, A.; Goellner, V.; Zitolo, A.; Fonda, E.; Donnadieu, B.; Jones, D.; Jaouen, F. Synergy between Molybdenum Nitride and Gold Leading to Platinum-like Activity for Hydrogen Evolution. *Phys. Chem. Chem. Phys.* **2015**, *17*, 4047–4053.

(25) Ramaswamy, N.; Tylus, U.; Jia, Q.; Mukerjee, S. Activity Descriptor Identification for Oxygen Reduction on Nonprecious Electrocatalysts: Linking Surface Science to

Coordination Chemistry. *J. Am. Chem. Soc.* **2013**, *135*, 15443–15449.

(26) Choi, C. H.; Baldizzone, C.; Grote, J. P.; Schuppert, A. K.; Jaouen, F.; Mayrhofer, K. J. J. Stability of Fe-N-C Catalysts in Acidic Medium Studied by Operando Spectroscopy. *Angew. Chemie - Int. Ed.* **2015**, *54*, 12753–12757.

(27) Gewirth, A. A.; Varnell, J. A.; DiAscro, A. M. Nonprecious Metal Catalysts for Oxygen Reduction in Heterogeneous Aqueous Systems. *Chem. Rev.* **2018**, *118*, 2313–2339.

(28) Choi, C. H.; Choi, W. S.; Kasian, O.; Mechler, A. K.; Sougrati, M. T.; Brüller, S.; Strickland, K.; Jia, Q.; Mukerjee, S.; Mayrhofer, K. J. J.; et al. Unraveling the Nature of Sites Active toward Hydrogen Peroxide Reduction in Fe-N-C Catalysts. *Angew. Chemie - Int. Ed.* **2017**, *56*, 8809–8812.

(29) Shao, M.; Chang, Q.; Dodelet, J. P.; Chenitz, R. Recent Advances in Electrocatalysts for Oxygen Reduction Reaction. *Chem. Rev.* **2016**, *116*, 3594–3657.

(30) Xie, J.; Xie, Y. Transition Metal Nitrides for Electrocatalytic Energy Conversion: Opportunities and Challenges. *Chem. - A Eur. J.* **2016**, *22*, 3588–3598.

(31) Zhong, H.; Zhang, H.; Liu, G.; Liang, Y.; Hu, J.; Yi, B. A Novel Non-Noble Electrocatalyst for PEM Fuel Cell Based on Molybdenum Nitride. *Electrochem. commun.* **2006**, *8*, 707–712.

(32) Chen, W. F.; Sasaki, K.; Ma, C.; Frenkel, A. I.; Marinkovic, N.; Muckerman, J. T.; Zhu, Y.; Adzic, R. R. Hydrogen-Evolution Catalysts Based on Non-Noble Metal Nickel-Molybdenum Nitride Nanosheets. *Angew. Chemie - Int. Ed.* **2012**, *51*, 6131–6135.

(33) Zhong, Y.; Xia, X.; Shi, F.; Zhan, J.; Tu, J.; Fan, H. J. Transition Metal Carbides and Nitrides in Energy Storage and Conversion. *Adv. Sci.* **2016**, *3*, 1500286.

(34) Cao, B.; Veith, G. M.; Diaz, R. E.; Liu, J.; Stach, E. A.; Adzic, R. R.; Khalifah, P. G.

Cobalt Molybdenum Oxynitrides: Synthesis, Structural Characterization, and Catalytic Activity for the Oxygen Reduction Reaction. *Angew. Chemie - Int. Ed.* **2013**, *52*, 10753–10757.

(35) Cao, B.; Neuefeind, J. C.; Adzic, R. R.; Khalifah, P. G. Molybdenum Nitrides as Oxygen Reduction Reaction Catalysts: Structural and Electrochemical Studies. *Inorg. Chem.* **2015**, *54*, 2128–2136.

(36) Butcher, K. S. A. The Oxygen Contamination Problem for Plasma Enhanced ALD and PECVD, 2015. http://www.meaglow.com/ (accessed Feb 20, 2020).

(37) Ishihara, A.; Tamura, M.; Ohgi, Y.; Matsumoto, M.; Matsuzawa, K.; Mitsushima, S.; Imai, H.; Ota, K. I. Emergence of Oxygen Reduction Activity in Partially Oxidized Tantalum Carbonitrides: Roles of Deposited Carbon for Oxygen-Reduction-Reaction-Site Creation and Surface Electron Conduction. *J. Phys. Chem. C* **2013**, *117*, 18837–18844.

(38) Chisaka, M.; Ando, Y.; Itagaki, N. Activity and Durability of the Oxygen Reduction Reaction in a Nitrogen-Doped Rutile-Shell on TiN-Core Nanocatalysts Synthesised via Solution-Phase Combustion. *J. Mater. Chem. A* **2016**, *4*, 2501–2508.

(39) Ohgi, Y.; Ishihara, A.; Matsuzawa, K.; Mitsushima, S. Factors for Improvements of Catalytic Activity of Zirconium. **2013**, *160* (2), 162–167.

(40) Anitha, V. P.; Vitta, S.; Major, S. Structure and Properties of Reactively Sputtered γ-Mo2N Hard Coatings. *Thin Solid Films* **1994**, *245*, 1–3.

(41) Anitha, V. P.; Bhattacharya, A.; Patil, N. G.; Major, S. Study of Sputtered Molybdenum Nitride as a Diffusion Barrier. *Thin Solid Films* **1993**, *236*, 306–310.

(42) Chuang, J. C.; Tu, S. L.; Chen, M. C. Sputter-Deposited Mo and Reactively Sputter-Deposited Mo-N Films as Barrier Layers against Cu Diffusion. *Thin Solid Films* **1999**,

346, 299–306.

(43) Lee, J. Y.; Jeon, S. R.; Park, J. W. Effect of Deposition Conditions on the Physical and Electrical Properties of Reactive Sputtered Molybdenum Nitride Film. *J. Mater. Sci. Lett.* **1996**, *15*, 1495–1497.

(44) Inumaru, K.; Baba, K.; Yamanaka, S. Synthesis and Characterization of Superconducting β-Mo2N Crystalline Phase on a Si Substrate: An Application of Pulsed Laser Deposition to Nitride Chemistry. *Chem. Mater.* **2005**, *17*, 5935–5940.

(45) Stöber, L.; Konrath, J. P.; Haberl, V.; Patocka, F.; Schneider, M.; Schmid, U. Nitrogen Incorporation in Sputter Deposited Molybdenum Nitride Thin Films. *J. Vac. Sci. Technol. A Vacuum, Surfaces, Film.* **2016**, *34* (2), 021513.

(46) Maoujoud, M.; Binst, L.; Delcambe, P.; Offergeld-Jardinier, M.; Bouillon, F. Deposition Parameter Effects on the Composition and the Crystalline State of Reactively Sputtered Molybdenum Nitride. *Surf. Coatings Technol.* **1992**, *52* (2), 179–185.

(47) Ozsdolay, B. D.; Balasubramanian, K.; Gall, D. Cation and Anion Vacancies in Cubic Molybdenum Nitride. *J. Alloys Compd.* **2017**, *705*, 631–637.

(48) Wang, Y.; Lin, R. Y. Amorphous Molybdenum Nitride Thin Films Prepared by Reactive Sputter Deposition. *Mater. Sci. Eng. B* **2004**, *112*, 42–49.

(49) Jauberteau, I.; Bessaudou, A.; Mayet, R.; Cornette, J.; Jauberteau, J.; Carles, P.; Merle-Méjean, T. Molybdenum Nitride Films: Crystal Structures, Synthesis, Mechanical, Electrical and Some Other Properties. *Coatings* **2015**, *5*, 656–687.

(50) Haberkorn, N.; Bengio, S.; Suárez, S.; Pérez, P. D.; Sirena, M.; Guimpel, J. Effect of the Nitrogen-Argon Gas Mixtures on the Superconductivity Properties of Reactively Sputtered Molybdenum Nitride Thin Films. *Mater. Lett.* **2018**, *215*, 15–18.

(51) Shen, Y. G. Effect of Deposition Conditions on Mechanical Stresses and Microstructure of Sputter-Deposited Molybdenum and Reactively Sputter-Deposited Molybdenum Nitride Films. *Mater. Sci. Eng. A* **2003**, *359*, 158–167.

(52) Klimashin, F. F.; Koutná, N.; Euchner, H.; Holec, D.; Mayrhofer, P. H. The Impact of Nitrogen Content and Vacancies on Structure and Mechanical Properties of Mo-N Thin Films. *J. Appl. Phys.* **2016**, *120*, 185301.

(53) Balasubramanian, K.; Huang, L.; Gall, D. Phase Stability and Mechanical Properties of $Mo_{1-x}N_x$ with $0 \leq x \leq 1$. *J. Appl. Phys.* **2017**, *122* (19), 195101.

(54) Qi, J.; Jiang, L.; Jiang, Q.; Wang, S.; Sun, G. Theoretical and Experimental Studies on the Relationship between the Structures of Molybdenum Nitrides and Their Catalytic Activities toward the Oxygen Reduction Reaction. *J. Phys. Chem. C* **2010**, *114*, 18159–18166.

(55) Henss, A.; Rohnke, M.; Knaack, S.; Kleine-Boymann, M.; Leichtweiss, T.; Schmitz, P.; El Khassawna, T.; Gelinsky, M.; Heiss, C.; Janek, J. Quantification of Calcium Content in Bone by Using ToF-SIMS-a First Approach. *Biointerphases* **2013**, *8* (31), 1–8.

(56) Calvin, S. *XAFS for Everyone*; CRC Press: Boca Raton, FL, 2013.

(57) Koutna, N.; Holec, D.; Svoboda, O.; Klimashin, F. F.; Mayrhofer, P. H. Point Defects Stabilise Cubic Mo-N and Ta-N. *J. Phys. D. Appl. Phys.* **2016**, *49*, 375303.

(58) Shen, Y. G.; Mai, Y.-W. Reactively Sputter-Deposited Mo-Ox-Ny Thin Films. *Mater. Sci. Eng. B* **2002**, *95* (2002), 222–229.

(59) Liu, Z.; Meng, M.; Fu, Y.; Jiang, M.; Hu, T.; Xie, Y.; Liu, T. EXAFS Study of γ-Mo2N and Mo Nitrides Supported on Zeolites. *Mater. Lett.* **2002**, *54*, 364–371.

(60) Hones, P.; Martin, N.; Regula, M.; Levy, F. Structural and Mechanical Properties of

Chromium Nitride, Molybdenum Nitride, and Tungsten Nitride Thin Films. *J. Phys. D Appl. Phys* **2003**, *36* (8), 1023–1029.

(61) Liu, T.-C. Behavior of Molybdenum Nitrides as Materials for Electrochemical Capacitors. *J. Electrochem. Soc.* **1998**, *145* (6), 1882.

(62) Henke, B. L.; Gullikson, E. M.; Davis, J. C. X-Ray Interactions: Photoabsorption, Scattering, Transmission, and Reflection at E = 50-30,000 EV, Z = 1-92. *At. Data Nucl. Data Tables* **1993**, *54*, 181–342.

(63) Zhou, R.; Zheng, Y.; Jaroniec, M.; Qiao, S.-Z. Determination of the Electron Transfer Number for the Oxygen Reduction Reaction: From Theory to Experiment. *ACS Catal.* **2016**, *6* (7), 4720–4728.

(64) Wei, C.; Rao, R. R.; Peng, J.; Huang, B.; Stephens, I. E. L.; Risch, M.; Xu, Z. J.; Shao-Horn, Y. Recommended Practices and Benchmark Activity for Hydrogen and Oxygen Electrocatalysis in Water Splitting and Fuel Cells. *Adv. Mater.* **2019**, *31*, 1806296.

(65) Liu, Y.; Quan, X.; Fan, X.; Wang, H.; Chen, S. High-Yield Electrosynthesis of Hydrogen Peroxide from Oxygen Reduction by Hierarchically Porous Carbon. *Angew. Chemie - Int. Ed.* **2015**, *54*, 6837–6841.

(66) Bonakdarpour, A.; Esau, D.; Cheng, H.; Wang, A.; Gyenge, E.; Wilkinson, D. P. Preparation and Electrochemical Studies of Metal – Carbon Composite Catalysts for Small-Scale Electrosynthesis of H2O2. *Electrochim. Acta* **2011**, *56*, 9074–9081.

(67) Fellinger, T.; Hasche, F.; Strasser, P.; Antonietti, M. Mesoporous Nitrogen-Doped Carbon for the Electrocatalytic Synthesis of Hydrogen Peroxide. *J. Am. Chem. Soc.* **2012**, *134*, 4072–4075.

(68) Sun, Y.; Sinev, I.; Ju, W.; Bergmann, A.; Dresp, S.; Kuhl, S.; Spori, C.; Schmies, H.;

Wang, H.; Bernsmeier, D.; et al. Efficient Electrochemical Hydrogen Peroxide Production from Molecular Oxygen on Nitrogen-Doped Mesoporous Carbon Catalysts. *ACS Catal.* **2018**, *8*, 2844–2856.

(69) Jirkovský, J. S.; Panas, I.; Ahlberg, E.; Halasa, M.; Romani, S.; Schiffrin, D. J. Single Atom Hot-Spots at Au-Pd Nanoalloys for Electrocatalytic H2O2 Production. *J. Am. Chem. Soc.* **2011**, *133* (48), 19432–19441.

(70) Verdaguer-Casadevall, A.; Deiana, D.; Karamad, M.; Siahrostami, S.; Malacrida, P.; Hansen, T. W.; Rossmeisl, J.; Chorkendorff, I.; Stephens, I. E. L. Trends in the Electrochemical Synthesis of H2O2: Enhancing Activity and Selectivity by Electrocatalytic Site Engineering. *Nano Lett.* **2014**, *14*, 1603–1608.

(71) Wang, Y. L.; Gurses, S.; Felvey, N.; Boubnov, A.; Mao, S. S.; Kronawitter, C. X. In Situ Deposition of Pd during Oxygen Reduction Yields Highly Selective and Active Electrocatalysts for Direct H2O2 Production. *ACS Catal.* **2019**, *9*, 8453–8463.

(72) Gao, J.; Yang, H. bin; Huang, X.; Hung, S.-F.; Cai, W.; Jia, C.; Miao, S.; Chen, H. M.; Yang, X.; Huang, Y.; et al. Enabling Direct H2O2 Production in Acidic Media through Rational Design of Transition Metal Single Atom Catalyst. *Chem* **2020**, *6*, 1–17.

(73) Scholz, J.; Risch, M.; Stoerzinger, K. A.; Wartner, G.; Shao-Horn, Y.; Jooss, C. Rotating Ring-Disk Electrode Study of Oxygen Evolution at a Perovskite Surface: Correlating Activity to Manganese Concentration. *J. Phys. Chem. C* **2016**, *120* (49), 27746–27756.

(74) Nicholson, R. S. Theory and Application of Cyclic Voltammetry for Measurement of Electrode Reaction Kinetics. *Anal. Chem.* **1965**, *37* (11), 1351–1355.

(75) Eng, A. Y. S.; Ambrosi, A.; Sofer, Z.; Simek, P.; Pumera, M. Electrochemistry of Transition Metal Dichalcogenides: Strong Dependence on the Metal-to-Chalcogen

Composition and Exfoliation Method. *ACS Nano* **2014**, *8* (12), 12185–12198.

(76) Trasatti, S.; Petrii, O. A. Real Surface Area Measurements in Electrochemistry. *J. Electroanal. Chem.* **1992**, *327*, 353–376.

(77) Liu, T.-C.; Pell, W. G.; Conway, B. E.; Roberson, S. L. Behavior of Molybdenum Nitrides as Materials for Electrochemical Capacitors. *J. Electrochem. Soc.* **1998**, *145* (6), 1882–1888.

(78) McCrory, C. C. L.; Jung, S.; Peters, J. C.; Jaramillo, T. F. Benchmarking Heterogeneous Electrocatalysts for the Oxygen Evolution Reaction. *J. Am. Chem. Soc.* **2013**, *135*, 16977–16987.

(79) Gray, B. M.; Hector, A. L.; Jura, M.; Owen, R.; Whittam, J. Effect of Oxidative Surface Treatments on Charge Storage at Titanium Nitride Surfaces for Supercapacitor Applications. *J. Mater. Chem. A* **2017**, *5*, 4550–4559.

(80) Zhou, Y.; Guo, W.; Li, T. A Review on Transition Metal Nitrides as Electrode Materials for Supercapacitors. *Ceram. Int.* **2019**, *45*, 21062–21076.

(81) Ngamchuea, K.; Eloul, S.; Tschulik, K.; Compton, R. G. Planar Diffusion to Macro Disc Electrodes—what Electrode Size Is Required for the Cottrell and Randles-Sevcik Equations to Apply Quantitatively? *J. Solid State Electrochem.* **2014**, *18*, 3251–3257.

(82) McKenna, K. P. Structure, Electronic Properties, and Oxygen Incorporation/Diffusion Characteristics of the Σ 5 TiN(310)[001] Tilt Grain Boundary. *J. Appl. Phys.* **2018**, *123*, 075301.

(83) Wygant, B. R.; Kawashima, K.; Mullins, C. B. Catalyst or Precatalyst? The Effect of Oxidation on Transition Metal Carbide, Pnictide, and Chalcogenide Oxygen Evolution Catalysts. *ACS Energy Lett.* **2018**, *3*, 2956–2966.

(84) Schweitzer, G. K.; Pesterfield, L. L. *The Aqueous Chemistry of the Elements*; Oxford University Press: New York, 2010.

(85) Toney, M. F.; Brennan, S. Observation of the Effect of Refraction on x Rays Diffracted in a Grazing-Incidence Asymmetric Bragg Geometry. *Phys. Rev. B* **1989**, *39* (11), 7963–7966.

(86) Ravel, B.; Newville, M. ATHENA, ARTEMIS, HEPHAESTUS: Data Analysis for X-Ray Absorption Spectroscopy Using IFEFFIT. *J. Synchrotron Radiat.* **2005**, *12*, 537–541.

(87) Hellenbrandt, M. The Inorganic Crystal Structure Database (ICSD) - Present and Future. *Crystallogr. Rev.* **2014**, *10*, 17–21.

(88) Bravman, J. C.; Sinclair, R. The Preparation of Cross-Section Specimens for Transmission Electron Microscopy. *J. Electron Microsc. Tech.* **1984**, *1*, 53–61.

(89) Bard, A. J.; Faulkner, L. R. *Electrochemical Methods Fundamentals and Applications*, 2nd ed.; Harris, D., Swain, E., Robey, C., Aiello, E., Eds.; John Wiley & Sons: New York, 2001.

(90) Kresse, G.; Furthmüller, J. Efficient Iterative Schemes for Ab Initio Total-Energy Calculations Using a Plane-Wave Basis Set. *Phys. Rev. B* **1996**, *54* (16), 11169–11186.

(91) Hammer, B.; Hansen, L. B.; Nørskov, J. K. Improved Adsorption Energetics within Density-Functional Theory Using Revised Perdew-Burke-Ernzerhof Functionals. *Phys. Rev. B* **1999**, *59* (11), 7413–7421.

(92) Blöchl, P. E. Projector Augmented-Wave Method. *Phys. Rev. B* **1994**, *50* (24), 17953–17979.

1
2

1 TOC Image

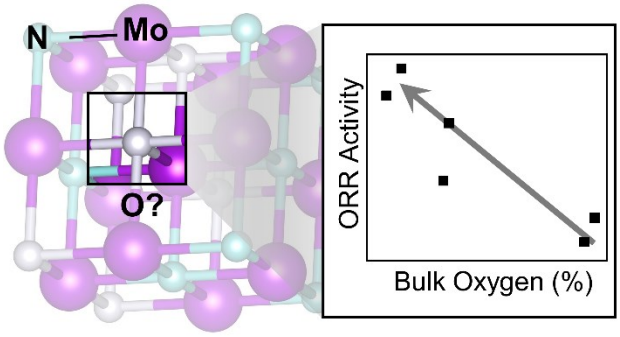

2